JACS
JOURNAL OF THE AMERICAN CHEMICAL SOCIETY
Article
pubs.acs.org/JACS

Spectroscopic and Reactivity Comparisons between Nonheme Oxoiron(IV) and Oxoiron(V) Species Bearing the Same Ancillary Ligand

Valeria Dantignana,[†] Joan Serrano-Plana,[†,∥] Apparao Draksharapu,[‡,⊥] Carla Magallón,[†] Saikat Banerjee,[‡] Ruixi Fan,[§] Ilaria Gamba,[†] Yisong Guo,[§] Lawrence Que, Jr.,*[,‡] Miquel Costas,*[,†] and Anna Company*[,†]

[†]Institut de Química Computacional i Catàlisi (IQCC), Departament de Química, Universitat de Girona, C/M. Aurèlia Capmany 69, 17003 Girona, Catalonia, Spain

[‡]Department of Chemistry and Center for Metals in Biocatalysis, University of Minnesota, Minneapolis, Minnesota 55455, United States

[§]Department of Chemistry, Carnegie Mellon University, 4400 Fifth Avenue, Pittsburgh, Pennsylvania 15213, United States

Supporting Information

ABSTRACT: This work directly compares the spectroscopic and reactivity properties of an oxoiron(IV) and an oxoiron(V) complex that are supported by the same neutral tetradentate N-based $PyNMe_3$ ligand. A complete spectroscopic characterization of the oxoiron(IV) species (**2**) reveals that this compound exists as a mixture of two isomers. The reactivity of the thermodynamically more stable oxoiron(IV) isomer (**2b**) is directly compared to that exhibited by the previously reported 1e$^-$-oxidized analogue $[Fe^V(O)(OAc)(PyNMe_3)]^{2+}$ (**3**). Our data indicates that **2b** is 4 to 5 orders of magnitude slower than **3** in hydrogen atom transfer (HAT) from C−H bonds. The origin of this huge difference lies in the strength of the O−H bond formed after HAT by the oxoiron unit, the O−H bond derived from **3** being about 20 kcal·mol^{-1} stronger than that from **2b**. The estimated bond strength of the Fe^{IV}O−H bond of 100 kcal·mol^{-1} is very close to the reported values for highly active synthetic models of compound I of cytochrome P450. In addition, this comparative study provides direct experimental evidence that the lifetime of the carbon-centered radical that forms after the initial HAT by the high valent oxoiron complex depends on the oxidation state of the nascent Fe−OH complex. Complex **2b** generates long-lived carbon-centered radicals that freely diffuse in solution, while **3** generates short-lived caged radicals that rapidly form product C−OH bonds, so only **3** engages in stereoretentive hydroxylation reactions. Thus, the oxidation state of the iron center modulates not only the rate of HAT but also the rate of ligand rebound.

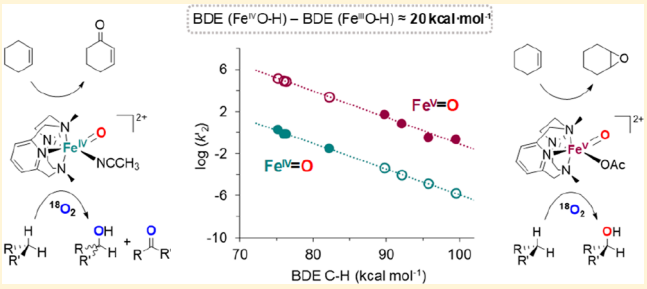

INTRODUCTION

High valent oxoiron species are the oxidizing agents in a variety of iron-dependent oxygenases. For example, in the heme enzyme cytochrome P450, a high-valent oxoiron(IV)-porphyrin radical (Cpd I) is responsible for the hydroxylation of aliphatic C−H bonds and of arene moieties,[1] as well as the epoxidation of olefins, among other reactions.[2−4] In Rieske oxygenases, a family of bacterial nonheme iron enzymes,[5,6] a yet undetected oxoiron(V) species has been proposed as the oxidizing agent,[7] while an S = 2 oxoiron(IV) species breaks strong C−H bonds via hydrogen atom transfer (HAT) in other nonheme oxygenases[8] such as taurine dioxygenase,[9] prolyl hydroxylase,[10] tyrosine hydroxylase,[11] phenyl alanine hydroxylase,[12] as well as in α-ketoglutarate dependent halogenases.[13−15] Due to the biological relevance of these high valent oxoiron compounds, intense research efforts have been devoted to the preparation of synthetic analogues that can reproduce both the structural properties and the reactivity of the biological systems. These synthetic models aim to provide detailed insight into the enzymatic mechanisms, and helpful information for the design of catalysts with potential application in environmentally friendly oxidation technologies.[16−20]

Resulting from these research efforts, a large number of synthetic oxoiron(IV) complexes has been described.[16] The reported systems typically consist of iron complexes based on tetra- and pentadentate nitrogen-based ligands, although complexes incorporating O atom donors[16,18] or organometallic moieties are also known.[21] Reactivity studies have disclosed that in most cases these synthetic oxoiron(IV) complexes are competent to perform hydrogen-atom abstraction of weak C−

Received: June 4, 2019
Published: August 30, 2019

DOI: 10.1021/jacs.9b05758
J. Am. Chem. Soc. XXXX, XXX, XXX−XXX

H bonds and oxygen atom transfer (OAT) to sulfides. Examples in which such species can break stronger C−H bonds are scarce, and moderate reaction rates are observed in most of these cases.[22]

In sharp contrast to the plentiful examples of well-defined synthetic oxoiron(IV) species, the preparation of the one-electron oxidized oxoiron(V) analogues has remained elusive. This can be attributed to the higher oxidizing abilities of these species that make them especially reactive and thus difficult to trap. The first example of a nonporphyrinic oxoiron(V) complex was reported by Collins and co-workers using a tetraanionic macrocyclic tetramide ligand (TAML).[23] $[Fe^{V}(TAML)(O)]^{-}$ was characterized by several spectroscopic means, and reactivity studies demonstrated that it was competent in OAT to sulfides and alkenes and in HAT from alkanes.[23,24] The structurally related compound $[Fe^{V}(bTAML)(O)]^{-}$ was reported a few years later, and it exhibited remarkably higher stability at room temperature.[25,26] Nevertheless, these oxoiron(V) species are far less reactive than cytochrome P450 Cpd I,[27] which is considered as their biological heme analogue, suggesting that the tetraanionic character of TAML and related ligands attenuate the electrophilicity of the complex, significantly limiting their oxidation reactivity.

It was recently reported that the reaction of peracids with the iron(II) complex bearing a neutral N-based $PyNMe_3$ ligand, $[Fe^{II}(PyNMe_3)(CH_3CN)_2]^{2+}$ (**1**, Scheme 1), generates

Scheme 1. Structure for Complex 1 and Synthesis of the Corresponding Oxoiron(IV) (2b) and Oxoiron(V) (3) Complexes

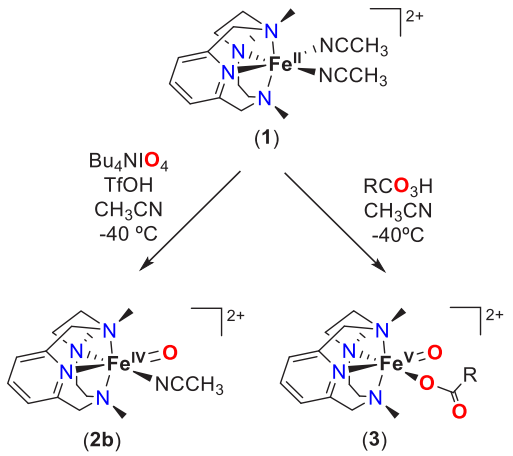

an oxoiron(V) species, $[Fe^{V}(O)(OAc)(PyNMe_3)]^{2+}$ (**3**, Scheme 1),[22,28] which exhibits fast reaction rates in the stereoretentive hydroxylation of unactivated C−H bonds of alkanes[5] and in the epoxidation of olefins,[6] even approaching the values reported for P450 Cpd I. The exact electronic structure of **3** has been a matter of debate. Münck, Costas and Que, on the basis of a thorough spectroscopic data, describe the species as an oxoiron(V) core attached to carboxylate ligand, generated after heterolytic O−O cleavage of a cyclic iron(III)-peracetate moiety.[28] In contrast, Ye, Neese, and co-workers claim that the compound is best characterized as an iron(IV) center antiferromagnetically coupled to an O−O radical, so that O−O bond has not been completely broken.[29] Thus, this is a fascinating molecule with a very intriguing electronic structure. However, the interest in compound **3** goes beyond its unique bonding structure, as it shows reaction rates and selectivity patterns fully congruent with those of related iron complexes used as efficient catalysts in C—H and C=C oxidation reactions. Indeed, low temperature EPR studies performed along the catalytic reactions of some of these related systems during catalysis display the transient formation of small (<2%) amounts of species with the characteristic spectroscopic features of **3**.[30−33] These data strongly suggest that **3** may constitute a representative example of the oxidizing agents operating with these catalysts.[20,34]

In this work, the spectroscopic and reactivity properties of **3** are compared with those of its oxoiron(IV) counterpart $[Fe^{IV}(O)(PyNMe_3)(CH_3CN)]^{2+}$ (**2**). This oxoiron(IV) species has been characterized by several spectroscopic techniques and, remarkably, two isomers can be identified. The HAT and OAT reactivity of the more thermodynamically stable isomer (**2b**, Scheme 1) has been studied and compared to **3**. By comparing the reactivity of these two complexes with the same tetradentate ligand architecture, the current work provides valuable insight into the impact of the iron oxidation state in defining the unusual reactivity properties of **3**.

RESULTS AND DISCUSSION

Synthesis and Characterization of 2. The oxoiron(IV) complex $[Fe^{IV}(O)(PyNMe_3)(CH_3CN)]^{2+}$ (**2**) can be prepared by reaction of the iron(II) precursor $[Fe^{II}(PyNMe_3)(CH_3CN)_2]^{2+}$ (**1**) in CH_3CN with either 1.1 equiv Bu_4NIO_4 or 4 equiv 2-*t*$BuSO_2$−C_6H_4IO, albeit with low yields (∼40%) as previously determined by Mössbauer spectroscopy.[28] However, the addition of 0.8 equiv triflic acid (TfOH) or 1 equiv $HClO_4$ together with 1.1 equiv Bu_4NIO_4 to **1** affords the target complex **2** with significantly higher yields, as determined by the increased intensity of the two absorption bands characteristic of **2** at ∼800 and ∼980 nm.[35]

UV−vis spectral monitoring of the generation of **2** shows that the relative intensities of these two low energy bands change over time (Figure 1. Thus, the initially more intense ∼800 nm band decreases concomitantly with the increase in the intensity of the ∼980 nm band, which then becomes the more intense of the two near-IR bands (Figure 1. These

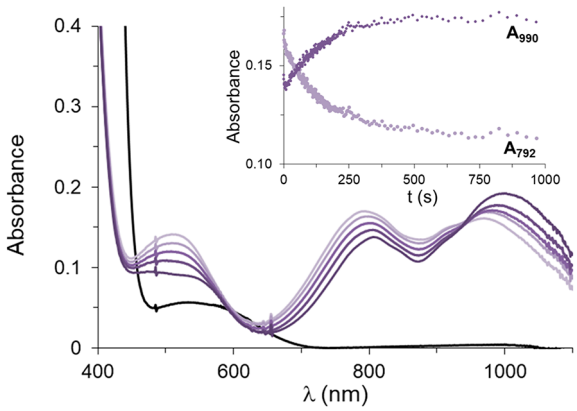

Figure 1. Spectral changes occurring upon reaction of a solution of **1** (1 mM, black line) in CH_3CN with 1.1 equiv Bu_4NIO_4 and 0.8 equiv TfOH at −40 °C. Two bands at ∼800 and ∼980 nm are immediately formed upon mixing the reactants, but their relative intensities changes over time. Inset: kinetic traces at 792 and 990 nm.

DOI: 10.1021/jacs.9b05758
J. Am. Chem. Soc. XXXX, XXX, XXX−XXX

Table 1. Summary of Spectroscopic Data for 2a, 2b, and 3

		2a	2b	3[c]
UV–vis–NIR	λ_{max}, nm (ε, $M^{-1}cm^{-1}$)	792 (–)[a]	805 (230)[b]	490 (4500)[b]
		970 (–)[a]	990 (320)[b]	680 (sh)
Mössbauer	δ, mm/s (ΔE_Q, mm/s)	0.07 (0.98)	0.09 (0.24)	−0.06 (1.00)
rRaman	ν (Fe–O), cm^{-1}	822	829	815
XAS	K-edge energy, eV	7124.8	7124.4	7124.8
	pre-edge energy, eV	7114.1	7114.0	7114.4
	pre-edge area, units	20.9	19.6	15.6
	r(Fe═O), Å	1.66	1.65	1.63
	average r(Fe–N), Å	2.00	2.00	1.97[d]

[a]Reliable extinction coefficient for **2a** could not be obtained due to the unavoidable contamination of this compound by **2b**. [b]Extinction coefficient values (ε) determined from the purity calculated by Mössbauer (for **2b**) or EPR analyses (for **3**). [c]Spectroscopic data for **3** was obtained from refs 22, 28. Mössbauer and XAS parameters were obtained from samples of **3** generated using cyclohexyl peroxycarboxylic acid instead of peracetic acid. [d]A second Fe–N subshell is observed at 2.17 Å, which we assign to Fe–N bonds of the diferric byproduct, that represents 50% of the Fe in samples of **3**.

observations suggest that two species are formed along the reaction pathway and an isosbestic point at 940 nm becomes apparent in the conversion between them. Interestingly, when the reaction of **1** with IO_4^-/TfOH is performed at −60 °C using a 1:1 CH_3CN:CH_2Cl_2 solvent mixture, the initial compound (**2a**) remains stable at this temperature. However, when the same reaction is carried out at −20 °C, the direct formation of the second species (**2b**) is observed (Figure S8).

Spectroscopic analyses have been carried out in order to validate the iron oxidation states of **2a** and **2b** and characterize their electronic structures (Table 1). Mössbauer samples of the two species were prepared by freezing the reaction mixture of ^{57}Fe-enriched **1** and the oxidant in CD_3CN at −40 °C to obtain samples of the initial and final species (**2a** and **2b**, Figure 2). Besides unavoidable high-spin ferric impurities that represented ∼35% of the samples, the Mössbauer spectra showed time-dependent patterns for the two species that can be clearly characterized by two doublets with different quadrupole splittings. While the sample obtained at reaction time t = 2 min consists of 35% of the kinetically favored species **2a** and 30% of the thermodynamically favored species **2b**, **2a** eventually converts into **2b** at t = 30 min. The Mössbauer parameters of species **2b** (δ = 0.09 mm/s, ΔE_Q = 0.24 mm/s) are fully consistent with its assignment to an S = 1 oxoiron(IV) species previously reported by some of us.[28] Interestingly, the initial species formed with λ_{max} at ∼800 nm (**2a**) exhibits different Mössbauer parameters that are also consistent with an oxoiron(IV) species (δ = 0.07 mm/s, ΔE_Q = 0.98 mm/s) with a larger ΔE_Q relative to **2b**. Several attempts to avoid contamination of **2a** by **2b** were carried out, but they all proved unsuccessful, perhaps because of the relatively low energy barrier for conversion of **2a** to **2b**.

Resonance Raman experiments (λ_{exc} = 457 nm) of frozen acetonitrile solutions at 77 K also showed distinct parameters for **2a** and **2b** (Figure 3). A resonantly enhanced band at 822 cm^{-1} was observed for **2a**, while a Raman band at 829 cm^{-1} was observed for **2b**. Both values fall in the range of the ν(Fe═O) modes (798–862 cm^{-1}) previously measured for oxoiron(IV) species.[36]

X-ray absorption spectroscopy (XAS) at 10 K was also used to characterize samples of **2a** and **2b** (Figure 4). The K-edge energies and pre-edge areas for samples of **2a** and **2b** were found to be 7124.8 eV and 20.9 units and 7124.4 eV and 19.6 units, respectively, in the typical range reported for S = 1 Fe^{IV}═O complexes.[36] The Fourier transformed EXAFS

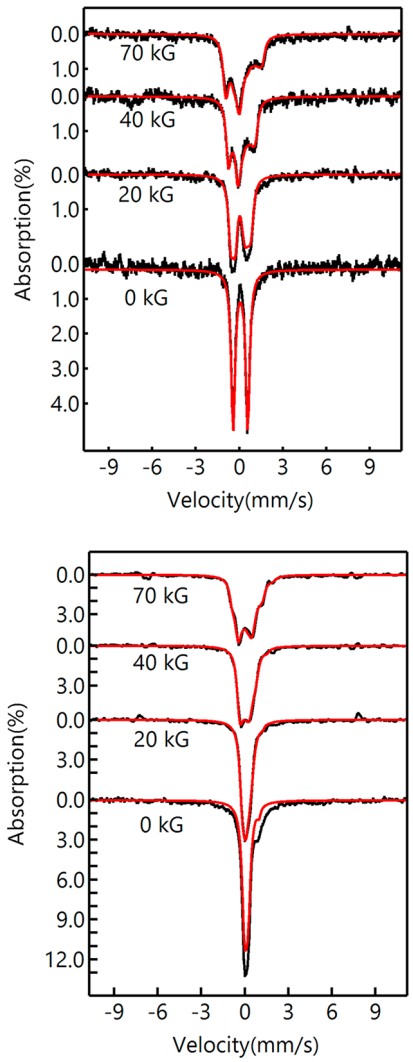

Figure 2. Mössbauer spectra of **2a** and **2b** at various temperatures and magnetic fields. The stacked spectra in the top panel were recorded from the sample frozen at t = 2 min. The high-spin ferric species and species **2b** have been removed to highlight the pattern for species **2a** (35% of total iron). The stacked spectra on the bottom panel were recorded from the sample frozen at t = 30 min. The high-spin ferric species has been removed to highlight the pattern of species **2b** (60% of total iron). Raw Mössbauer data can be found in Figure S6.

DOI: 10.1021/jacs.9b05758
J. Am. Chem. Soc. XXXX, XXX, XXX–XXX

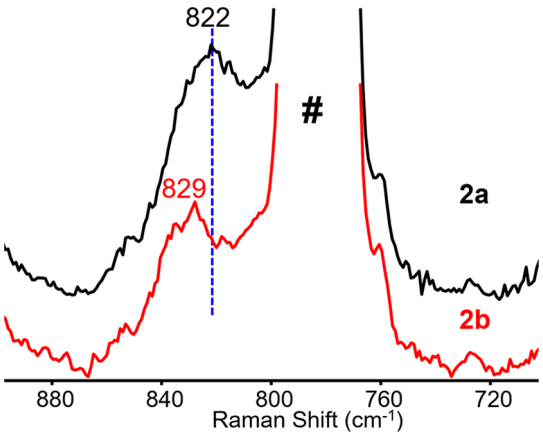

Figure 3. Resonance Raman spectra of **2a** (black line) and **2b** (red line) in frozen acetonitrile solutions at 77 K (λ_{exc} = 457 nm). Band marked with # corresponds to solvent.

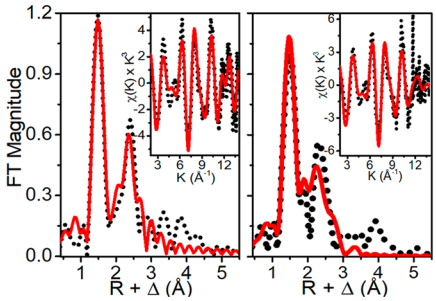

Figure 4. Fourier-transformed *k*-space EXAFS data of **2a** (left) and **2b** (right) in acetonitrile at 10 K. Insets show the *k*-space spectra.

spectrum of **2b** shows two major features at R + Δ ∼ 1.5 and 2.4 Å (Figure 4). The shell at R + Δ ∼ 1.5 is best fit with a 0.8 O scatterer at 1.65 Å that is typical for an Fe═O unit and 5 N/O scatterers at 2.0 Å arising from the ligand $PyNMe_3$ and probably from a coordinated CH_3CN. The latter shell is best fit with C scatterers at 2.9 and 3.04 Å that typically arise from pyridine containing ligands. The average Fe−N distance of 2.0 Å is as expected to an S = 1 Fe^{IV}═O species.[37] Species **2a** exhibits bond metrics similar to **2b** and the results are summarized in Table S3. Not surprisingly, XAS spectroscopy does not distinguish between the different compounds.

The two oxoiron(IV) complexes **2a** and **2b** may differ only in the nature of the ligand bound *cis* to the oxo atom, which may be the CH_3CN solvent, a $CF_3SO_3^-$ anion or IO_3^-/IO_4^- derived from the oxidant. In order to test the likelihood of anion binding, the reactants for the generation of the oxoiron(IV) species were modified: in one experiment the starting iron(II) complex **1** was replaced by $[Fe^{II}(PyNMe_3)(CH_3CN)_2](SbF_6)_2$ (**1·SbF$_6$**), which does not provide any coordinating anion, and in another experiment 2-*t*$BuSO_2$−C_6H_4IO was used as an oxidant instead of Bu_4NIO_4. In both cases, isomer **2a** is still initially formed and then evolves to **2b** in CH_3CN at −40 °C (Figures S10 and S11). Thus, $CF_3SO_3^-$, IO_3^- or IO_4^- coordination can be ruled out as the rationale for having two different oxoiron(IV) species, and a CH_3CN solvent molecule is the most likely to be bound to the labile site in **2a** and **2b**. The inequivalence of the two positions available for oxo coordination to the iron center, one *trans* to the pyridine and the other *trans* to an *N*-methyl group (see Scheme 2b) easily rationalizes the existence of two geometrical

Scheme 2. (a) Different Ligands (X) Can Be Coordinated *cis* to the Oxo Group in 2a and 2b; (b) Possible Structure of the Two Geometrical Isomers of the Oxoiron(IV) Species, 2a and 2b

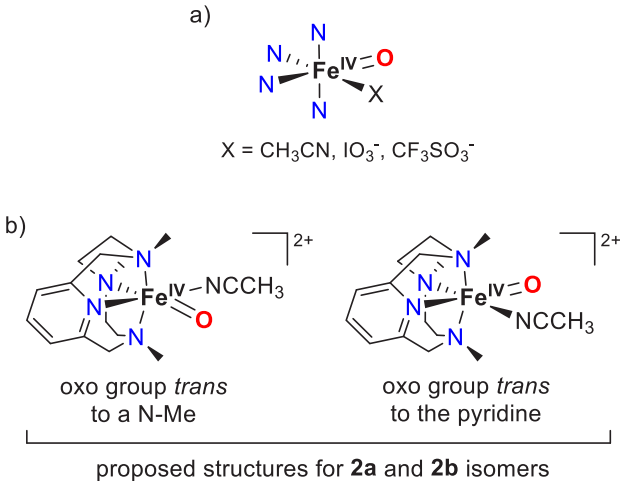

isomers. Thus, **2a** would be the kinetically favored geometric isomer that then evolves to the thermodynamic product **2b**. The existence of two geometrical isomers of oxoiron(IV) compounds with tetradentate ligands has been discussed in previous systems, but spectroscopic characterization of the two species has only been achieved with the equatorially bound tetramethylcyclam (TMC) ligand.[38−40]

Studies have shown that ^{1}H NMR spectroscopy can be a useful method for determining how the pyridine donors are bound relative to the Fe═O unit.[41−43] They could be coordinated either *cis* or *trans* to the oxo unit, and in the case of the *cis*-bound mode, the ring may be oriented parallel or perpendicular relative to the Fe═O axis or somewhere in between (Table 2). Indeed we show below that this technique can distinguish between the two geometrical isomers of **2**, as the orientation of the pyridine with respect to the Fe═O unit is different in the two options (Scheme 2b).

Table 2. ^{1}H NMR Paramagnetic Shifts Observed for Pyridine Protons of Oxoiron(IV) Complexes[a]

compound	T (K)	β	β'	γ	ref
$[Fe^{IV}(O)(N4Py)]^{2+}$	298	$\beta_{\parallel}$ 37	$\beta'_{\parallel}$ −24	$\gamma_{\parallel}$ 2.5	41
		$\beta_{\parallel}$ 23	$\beta'_{\parallel}$ −18	$\gamma_{\parallel}$ 1.3	
$[Fe^{IV}(O)(BnTPEN)]^{2+}$	298	$\beta_{\parallel}$ 36	$\beta'_{\parallel}$ −22.3	$\gamma_{\parallel}$ 3.6	41
		$\beta_{\parallel}$ 33	$\beta'_{\parallel}$ −21.7	$\gamma_{\parallel}$ 3.0	
		$\beta_{\perp}$ −7.3	$\beta'_{\perp}$ −8.5	$\gamma_{\perp}$ 1.4	
$[Fe^{IV}(O)(Py_2MeTACN)]^{2+}$	298	$\beta_{\parallel}$ 39	$\beta'_{\parallel}$ −20	$\gamma_{\parallel}$ 6.3	42
		$\beta_{\perp}$ −8.4	$\beta'_{\perp}$ −5.5	$\gamma_{\perp}$ 4.2	
$[Fe^{IV}(O)(TMC\text{-}py)]^{2+}$	298	β_{trans} 3.6, −0.5		γ_{trans} −11.6	44
$[Fe^{IV}(O)(PyNMe_3)(CH_3CN)]^{2+}$ (**2a**)	208	−26		5	this work
$[Fe^{IV}(O)(PyNMe_3)(CH_3CN)]^{2+}$ (**2b**)	208	8		−32	this work

[a]Relative to pyridine at 7 ppm.

DOI: 10.1021/jacs.9b05758
J. Am. Chem. Soc. XXXX, XXX, XXX−XXX

The ^{1}H NMR spectrum of the more stable **2b** isomer recorded at −65 °C in 1:1 CD_3CN/CD_2Cl_2 exhibits relatively sharp and well-resolved paramagnetically shifted signals due to the S = 1 Fe^{IV}═O center (Figure 5). The number of signals observed is consistent with the presence of a mirror plane of symmetry that bisects the pyridine ring. Due to their longer distances from the Fe center, the pyridine protons give rise to the sharpest signals in the spectrum of **2b**, which are found at −25 ppm (1H) and 15 ppm (2H) (Figure 5). These peaks can be assigned respectively to the single γ and the two β protons of the pyridine based on their relative intensities. The remaining broader spectral features can be reasonably associated with benzylic CH_2 (42 and −56 ppm), N−CH_2 (−35, −133 ppm) and N−CH_3 (−60 ppm) hydrogens, based on relative integrations of the resonances and by comparison to the ^{1}H NMR spectrum for the corresponding oxoiron(IV) species supported by the macrocyclic ligand with deuterated benzylic protons (**2b**-d_4) (Figure S7).

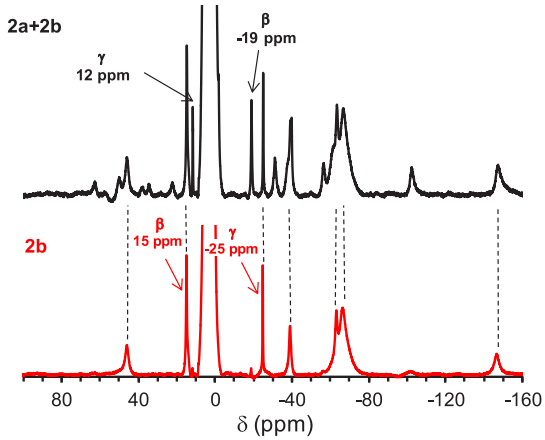

Figure 5. ^{1}H NMR spectra of a mixture of **2a** and **2b** (top) and **2b** (bottom) in 1:1 CD_3CN/CD_2Cl_2 at −65 °C. Pyridine β (2H) and γ (1H) protons are labeled in the figure. Other broader peaks for **2b** are assigned as follows: benzylic protons at 46 ppm (2H) and −63 ppm (2H), aliphatic CH_2 peaks at −39 ppm (2H) and −147 ppm (2H), and CH_3 protons at −67 ppm (9H).

The chemical shift pattern observed for the pyridine β and γ protons of **2b** can shed light on the orientation of the pyridine ligand relative to the Fe═O unit, based on comparisons with the patterns associated with structurally well characterized Fe^{IV}═O complexes in the literature.[43] Most published examples have pyridines bound *cis* to the Fe═O unit and oriented parallel to the Fe═O axis, namely $[Fe^{IV}(O)(N4Py)]^{2+}$, $[Fe^{IV}(O)(BnTPEN)]^{2+}$ and $[Fe^{IV}(O)(MePy_2tacn)]^{2+}$ (N4Py = *N*,*N*-bis(2-pyridyl-methyl)-*N*-bis(2-pyridyl)methylamine; BnTPEN = *N*-benzyl-*N*,*N*′,*N*′-tris(2-pyridylmethyl)-1,2-diaminoethane; $MePy_2tacn$ = *N*-methyl-*N*′,*N*″-bis(2-pyridylmethyl)-1,4,7-triazacyclononane).[41,42,45] Such pyridine rings exhibit β and β' protons respectively downfield and upfield shifted by 30−40 ppm and γ protons slightly downfield shifted from their respective diamagnetic positions. Besides having equatorial pyridines bound parallel to the Fe═O unit, both $[Fe^{IV}(O)(BnTPEN)]^{2+}$ and $[Fe^{IV}(O)(Py_2MeTACN)]^{2+}$ have an additional pyridine bound *cis* to the Fe═O unit but with the ring perpendicular to the Fe═O unit. These pyridine donors exhibit smaller paramagnetic shifts of ∼10 ppm upfield for the β protons and 4−14 ppm downfield for the γ proton.

Neither of the shift patterns described above matches that observed for **2b**, which exhibits a relatively small downfield paramagnetic shift of 8 ppm for the β protons and a larger upfield paramagnetic shift of 32 ppm for the γ proton. Such a pattern is associated with a pyridine bound *trans* to the oxo atom, as reported for the pendant pyridine ligand *trans* to the Fe═O unit in $[Fe^{IV}(O)(TMC\text{-}py)]^{2+}$ (TMC-py = 1-(pyridyl-2-methyl)-4,8,11-trimethyl-1,4,8,11-tetrazacyclotetradecane).[44] For the latter complex, the two pyridine β protons exhibit quite small paramagnetic shifts of −0.5 and +3.6 ppm (actual peaks observed at 6.5 and 10.6 ppm) and a larger paramagnetic shift of nearly −11.6 ppm for the γ proton found at −4.6 ppm. Although there is a difference in the magnitudes of the paramagnetic shifts of the pyridine protons between these two complexes, the directions of the shifts agree. The larger paramagnetic shifts observed for **2b** versus $[Fe^{IV}(O)(TMC\text{-}py)]^{2+}$ (Table 2) likely arise from two factors: (a) the 90 °C difference in temperature at which the NMR data were obtained, which will decrease when this difference is taken into account, and (b) the shorter Fe−N_{py} bond length of 2.03 Å calculated for **2b** (see Supporting Information, Figure S27, for more details) versus the 2.118(3) Å value determined crystallographically for $[Fe^{IV}(O)(TMC\text{-}py)]^{2+}$, which results in greater unpaired spin density delocalized onto the pyridine in the former.[46]

The ^{1}H NMR spectrum of **2a** in 1:1 CD_3CN:CD_2Cl_2 at −65 °C shows significant contamination from the more stable **2b** isomer, as shown by the Mössbauer results discussed earlier (Figure 2). On the basis of the above assignment of **2b** as the *trans* isomer, **2a** should correspond to the *cis* isomer with the pyridine perpendicular to the Fe═O axis. From a careful inspection of the composite **2a** + **2b** spectrum and comparison with the spectrum of pure **2b**, we can identify sharper features with a relative 2:1 intensity ratio at −19 and 12 ppm that we assign to the β and γ protons of **2a**, respectively. The shift pattern with upfield shifted β protons and a downfield shifted γ proton is fully consistent with a *cis*-bound pyridine perpendicular to the Fe═O unit (Scheme 2b), as found for the pyridines perpendicular to the Fe═O units of $[Fe^{IV}(O)(BnTPEN)]^{2+}$ and $[Fe^{IV}(O)(Py_2MeTACN)]^{2+}$ (Table 2).[41,42]

Interestingly, in line with the experimental observations, DFT calculations predict that the isomer with the oxo group *trans* to the pyridine ring is slightly energetically favored (by 0.9 kcal/mol) over the isomer with the oxo group *cis* to the pyridine (see Supporting Information for more details). This further supports the NMR results pointing out that the most stable isomer **2b** contains the pyridine *trans* to the oxo group, and they show a relative *cis* orientation in the kinetically favored geometric isomer **2a**.

Oxidative Reactivity of 2a versus 2b and Comparison to 3. The oxidizing abilities of **2a** and **2b** were compared at −60 °C. Isomer **2a** was directly synthesized at −60 °C in 1:1 CH_3CN:CH_2Cl_2. Of note, this compound is obtained together with approximately equimolar amounts of isomer **2b** according to spectroscopic studies (see above). Compound **2b** was first generated at −40 °C and then cooled down to −60 °C for reactivity comparisons with **2a**. Reaction rates were determined by monitoring the decay of the near-IR absorption bands characteristic of **2a** and **2b** (at 792 and 990 nm, respectively) upon addition of an excess of a particular substrate (Figure S12 and S13). In the case of **2b**, its decay at 990 nm could be fitted to single exponential functions, from which observed reaction rates (k_{obs}) and the corresponding

DOI: 10.1021/jacs.9b05758
J. Am. Chem. Soc. XXXX, XXX, XXX−XXX

second order rate constants (k_2) could be extracted. Reactions of **2a** with substrates were "contaminated" by the presence of approximately equimolar quantities of **2b**. Thus, the contribution of **2b** to the decay of the most intense absorption band of **2a** at 792 nm was subtracted to obtain the decay of "pure" compound **2a**. Gratifyingly, the reaction of this species with substrates could also be nicely fitted to a single exponential function and reaction rates for **2a** could be extracted (see Supporting Information for more details). Both species exhibited hydrogen-atom transfer (HAT) and oxygen atom transfer (OAT) reactivity typically observed for most S = 1 oxoiron(IV) complexes but they showed different reactivity trends. Isomer **2a** reacted approximately 18 times faster than **2b** in HAT reactions with 9,10-dihydroanthracene (k_2 = 9.5 M^{-1} s^{-1} for **2a** and 0.53 M^{-1} s^{-1} for **2b**) but was about 4 times less reactive than **2b** in OAT reactions with thioanisole (k_2 = 0.038 M^{-1} s^{-1} for **2a** and 0.14 M^{-1} s^{-1} for **2b**). These results further support the notion that **2a** and **2b** correspond to two different oxoiron(IV) species that exhibit different relative reactivity.

Further reactivity studies of the oxoiron(IV) species were carried out using isomer **2b**. On the one hand, this compound corresponds to the thermodynamic product, so that it can be obtained without contamination from **2a** and is thermally stable at −40 °C, which makes it easier to manipulate. On the other hand, the relative disposition of the oxo group *trans* to the pyridine in **2b** is also observed in **3**. For the latter, spectroscopic analysis did not show the presence of two different isomers,[28] and the detected signals were assigned to the isomer with the oxo group *trans* to the pyridine as it was slightly more stable than the corresponding *cis* isomer on the basis of DFT calculations. Thus, **2b** and **3** likely represent the same geometric isomer making reactivity comparisons more straightforward.

First, the reactivity of **2b** with thioanisole and its *para*-substituted derivatives (X = OMe, Me, Cl, CN) at −40 °C was evaluated. Upon substrate addition, the absorption bands associated with **2b** disappeared (Figure S14), and this decay was also accompanied by the recovery of the UV−vis spectroscopic features of **1** (Figure S16), which was ascertained by MS (Figure S17). Moreover, analysis of the oxidized products in the reaction with thioanisole revealed the formation of the corresponding sulfoxide in 54% yield with respect to **2b**. Under conditions of excess substrate, the decay of the absorption band of **2b** at 990 nm could be fitted to a single exponential and second-order rate constants could be extracted. As expected, the Hammett analysis supported the electrophilic character of **2b** (ρ = −1.77, Figure S15) as previously observed for other well-defined oxoiron(IV) complexes[38,47] (see SI for more details). The reaction of the oxoiron(V) species **3** with sulfides is exceedingly fast, and reaction rates could not be determined even when analyzed at −45 °C by stopped flow methods.

Therefore, a direct comparison between the OAT ability of **2b** and **3** cannot be made, but the accumulated data indicate that **2b** behaves like a common oxoiron(IV) complex, while under the same reaction conditions **3** exhibits extraordinarily fast OAT rates. Under the assumption that the possible contributions of spin state changes to these reactions are either (i) insignificant or (ii) are very similar for the two compounds, the comparison highlights the extreme electrophilicity of the Fe^{V}═O unit.

The HAT ability of **2b** was also measured by studying its reaction with hydrocarbons. In this case, kinetic studies were carried out at −40 °C in order to establish a direct comparison with the reaction rates reported for **3** at this temperature (see below).[22] Substrates with relatively weak C−H bonds (BDE = 75−85 kcal·mol^{-1}) were used, because substrates with stronger bonds turned out to be unreactive toward **2b** at this temperature. Due to the limited solubility of the chosen substrates (xanthene, 1,4-cyclohexadiene, 9,10-dihydroanthracene, and fluorene) in CH_3CN at −40 °C, reactions were run in a 1:1 CH_3CN:CH_2Cl_2 mixture. Reactions produce $[Fe^{III}(OH)(CF_3SO_3)(PyNMe_3)]^+$ (ascertained by MS, Figure S19) and organic products. Reactions were monitored by UV−vis absorption spectroscopy by following the decay of the band at 990 nm characteristic of **2b** upon addition of the substrate (Figure S18). Under these experimental conditions reactions showed pseudo-first-order behavior and second-order reaction rates (k_2) could be extracted by plotting the observed rate constants (k_{obs}) as a function of the substrate concentration (Figure S20). These rate constants were then adjusted for the reaction stoichiometry to yield k_2' based on the number of abstractable hydrogen atoms of substrates. As expected, reaction rates decreased with the increase of the C−H BDE and more interestingly the log(k_2') values correlated linearly with the C−H BDE values, giving a slope of approximately −0.25 (kcal/mol)$^{-1}$ (Figure S21).

HAT reactions with compound **2b** also exhibit a normal kinetic isotope effect (KIE), so deuterated substrates react more slowly than their protio analogues. Using xanthene-d_2 and 9,10-dihydroanthracene-d_4, KIE values of 24 and 28 were obtained, respectively (Figure S23).[48] These high values are commonly observed in HAT processes carried out by oxoiron(IV) complexes. For example, a KIE value of 36 (at -40 °C) was reported for the oxidation of xanthene with the oxoiron(IV) complex bearing the 13-TMC ligand[49] and a KIE value of 27 (at −15 °C) was described for the oxidation of 9,10-dihydroanthracene using the $[Fe^{IV}(O)(CH_3CN)$-(Pytacn)$]^{2+}$ complex.[38] Interestingly, these high KIE values are comparable to the large KIE determined for the S = 2 oxoiron(IV) intermediate J in TauD (KIE ∼50).[50,51] Altogether, the good correlation between reaction rates and C−H BDE values and the large KIE values provides strong evidence for a rate-determining HAT process in the reactions of hydrocarbons with **2b**.

Activation parameters for HAT reactions of **2b** with xanthene and cyclohexadiene were determined by measuring reaction rates between 273 and 233 K. The corresponding Eyring plot for xanthene afforded $\Delta H^{\ddagger}$ = 6.4 ± 0.6 kcal·mol^{-1} and $\Delta S^{\ddagger}$ = −27.2 ± 2.6 cal·K^{-1}·mol^{-1}, while $\Delta H^{\ddagger}$ = 7.3 ± 0.5 kcal·mol^{-1} and $\Delta S^{\ddagger}$ = −25.6 ± 2.1 cal·K^{-1}·mol^{-1} were determined for cyclohexadiene (Figure S24). These values are very close to the ones previously reported for the reaction of a tetracarbene ligated oxoiron(IV) with 1,4-cyclohexadiene and 9,10-dihydroanthracene.[52]

It has been observed that the reactivity of oxoiron(IV) complexes depends dramatically on the ligand set.[53−55] The combination of the above-described data for **2b** and the recently described reactivity of **3**[22] represents a unique opportunity to compare the oxidizing abilities of a pair of oxoiron(IV) and oxoiron(V) compounds bearing exactly the same ligand architecture. A first notable observation is that reactions with substrates bearing strong C−H bonds (BDE ∼89−100 kcal·mol^{-1}) can only be studied for **3** because **2b**

DOI: 10.1021/jacs.9b05758
J. Am. Chem. Soc. XXXX, XXX, XXX−XXX

does not appear to be powerful enough to carry out HAT reactions with these strong C−H bonds. On the other hand, rates for HAT reactions with substrates containing weak C−H bonds can only be measured for **2b**, because the reaction with **3** exhibited extremely fast reaction rates, too fast even at −40 °C to be extracted by stopped flow methods.[22] Therefore, reaction rates for a common substrate are not available.

In order to establish a quantitative comparison between reaction rates, we performed regression analyses of the log(k_2') vs BDE correlations experimentally determined for **2b** and **3**. Regression analyses provide correlation lines with a slope of −0.25 (kcal/mol)$^{-1}$ in both cases (using a linear free energy relationship a unitless slope of 0.34 is obtained in both cases. Figures S22). This coincidence in the slopes of these correlations strongly suggests that HAT of **2b** and **3** proceed via very similar transition states. Extrapolation of the straight lines obtained in these correlations permitted us to estimate hypothetical second order reaction rates for substrates containing strong C−H bonds in the case of **2b**, and for the fast reactions of **3** against substrates with weak C−H bonds. Results are shown in Figure 6 and Table 3. As anticipated, the

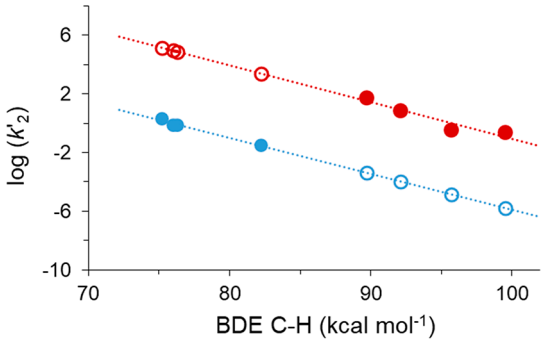

Figure 6. Correlation of log(k_2') with the BDE of different substrates at −40 °C for **2b** (blue line) and **3** (red line). Filled circles correspond to experimentally determined data and empty circles correspond to extrapolated values. The extrapolation made for compound **3** should be taken with a caveat, since a loss of linearity is likely to occur at BDE values below 90 kcal·mol^{-1}, as previously reported for other highly reactive HAT reagents (see text for more details).

Table 3. Experimental and Extrapolated k_2' Values for 2b and 3[a] at −40 °C

substrate	BDE (kcal mol^{-1})	compound **2b** k_2' (M^{-1} s^{-1})	compound **3** k_2' (M^{-1} s^{-1})
xanthene	75.2	2.1 ± 0.2	*1.4 × 10^5*
cyclohexadiene	76.0	0.70 ± 0.05	*8.7 × 10^4*
9,10-dihydroanthracene	76.3	0.77 ± 0.05	*7.4 × 10^4*
fluorene	82.2	0.030 ± 0.004	*2.5 × 10^3*
toluene	89.7	*4.2 × 10^{-4}*	55 ± 1[b]
tetrahydrofuran	92.1	*1.0 × 10^{-4}*	7.2 ± 0.2[b]
cyclooctane	95.7	*1.4 × 10^{-5}*	0.34 ± 0.01[b]
cyclohexane	99.5	*1.7 × 10^{-6}*	0.23 ± 0.01[b]

[a]Extrapolated values are shown in italics. [b]Ref 22.

gathered data show that **3** is four to 5 orders of magnitude more reactive than **2b**. It is important to note that extrapolation of the log(k_2') vs BDE correlations must be done with caution. While linear correlations over a wide range of BDEs have been reported for several oxoiron(IV) complexes with moderate reactivities,[25,38,55,56] a loss of linearity below 90 kcal/mol has been observed for a highly reactive peroxygenase compound I and *t*-butoxyl radicals.[27,57,58] Such a loss of linearity might not be discarded for the highly reactive oxoiron(V) species **3** for substrates with low BDEs, thus challenging the direct extrapolation at low BDEs for this compound. Thus, while loss of linearity may happen for compound **3** at low BDE values, this is not likely to occur at high BDEs for **2b** according to literature precedents. This way, extrapolation of the straight line is reliable for **2b** and the statement that **3** is four to 5 orders of magnitude more reactive than **2b** can be more strongly defended for strong C−H bonds.

Reactivity comparisons between oxoiron(IV) and oxoiron(V) species have been reported in very few systems. In fact, the only precedent for nonheme iron systems is for the complexes of the tetraanionic bTAML ligand. In this case, the reaction of [Fe^{V}(O)(bTAML)]$^{-}$ toward benzyl alcohol (BDE < 80 kcal·mol^{-1}) at pH 7 was found to be 2500 times faster than for its 1-e^{-}-reduced counterpart [Fe^{IV}(O)(bTAML)]$^{2-}$ at pH 12.[59] Of note, reactions toward stronger C−H bonds were precluded due to the attenuated electrophilicity of this system. In contrast, van Eldik and co-workers found that a Cpd I mimic, [(TMPS$^{\bullet+}$)Fe^{IV}(O)(H$_2$O)]$^{3-}$, reacted with benzyl alcohols only a hundred times faster than its 1-e^{-}-reduced counterpart [(TMPS)Fe^{IV}(O)(OH)]$^{5-}$. The different degrees of protonation of the OH/OH$_2$ ligand in these two compounds should be noted.[60] Even more interestingly, a Cpd I model compound reported by Groves [(4-TMPyP$^{\bullet+}$)-Fe^{IV}(O)]$^{+}$ exhibited a very high second order rate constant of 3.6 × 10^6 M^{-1} s^{-1} for the oxidation of xanthene, but negligible reactivity was observed when the 1-e^{-}-reduced analogue [(4-TMPyP)Fe^{IV}(O)] was used.[61] Indeed, the extrapolated reaction rate for the oxidation of xanthene calculated for **3** (Table 3) is only 10 times slower than that observed for Groves' model compound without accounting for the 50 °C difference in the measurements (reaction rates in the Groves' system were measured at +10 °C, while reactions for **3** were recorded at −40 °C), thus suggesting that **3** compares well in HAT reactivity with the most active cytochrome P450 mimics.

The KIE's determined for **2b** and **3** are also significantly different. **2b** exhibits very large KIE's (∼28), in agreement with the large values observed for synthetic and enzymatic oxoiron(IV) species, which are commonly rationalized on the basis of large tunneling contributions.[15,50,62,63] In contrast, KIE's determined for **3** of ∼5−6 are significantly smaller than those determined for **2b**, so they can still be accommodated by a classical treatment of the C−H cleavage. Notably, these "classical" values resemble those obtained for catalytic C−H oxidation systems with bioinspired iron catalysts.[64]

Activation parameters in representative HAT reactions performed by **2b** and **3** are collected in Table 4. Activation entropies are large and negative, consistent with a bimolecular process, and those determined for **2b** are systematically more negative. This pattern reflects a later and more ordered transition state for the less reactive **2b**. This provides some clues about the origin of the differences in the magnitude of the KIE's; tunneling contributions require close proximity between the hydrogen-donor and the hydrogen-acceptor and activation parameters indeed provide evidence for the necessary closer contact between the oxoiron(IV) (**2b**) and the substrate C−H bond with respect to the same situation in the more reactive oxoiron(V) (**3**).

DOI: 10.1021/jacs.9b05758
J. Am. Chem. Soc. XXXX, XXX, XXX−XXX

Table 4. Activation Parameters for the Reactions of 2b and 3 with C−H Bonds

compound	substrate	BDE (kcal mol^{-1})	$\Delta H^{\ddagger}$ (kcal mol^{-1})	$\Delta S^{\ddagger}$ (cal K^{-1} mol^{-1})	ref
2b	xanthene	75.2	6.4 ± 0.6	−27.2 ± 2.6	this work
	cyclohexadiene	76.0	7.3 ± 0.5	−25.6 ± 2.1	this work
3	toluene	89.7	6.5 ± 0.2	−19.6 ± 1.2	22
	cyclohexane	99.5	8.8 ± 0.7	−18.2 ± 1.9	22

The linear free energy correlation between log k'_2 and differences in enthalpy observed for the present system (Figure 6) provides interesting insights into the origin of the fast HAT reactivity of **3**. With few exceptions,[57,58,65] such a correlation is commonly observed for HAT reactions as described by the Bell−Evans−Polyani model.[66] The enthalpy change of the present reactions corresponds to the difference between the energy that is required to break the C−H bond (BDE_{C-H}) and the energy provided by the formation of the FeO−H bond (BDE_{FeO-H}) (eq 2). Considering that cyclohexadiene reacts with **2b** at a reaction rate (k_2' = 0.70 M^{-1} s^{-1}) that is only 2.05 times the rate of reaction of **3** with cyclooctane (k_2' = 0.34 M^{-1} s^{-1}), we can estimate that both reactions have similar activation free energies given the observed Bell−Evans−Polyani correlation (Figure 6). Therefore, the 20 kcal·mol^{-1} difference in BDE_{C-H} between these two substrates (76.0 kcal·mol^{-1} for cyclohexadiene and 95.7 kcal·mol^{-1} for cyclooctane) should approximately correspond to the difference in energy between the BDE of $Fe^{III}O-H$ and $Fe^{IV}O-H$.

$$Fe^{n+}{=}O + C{-}H \xrightarrow[\text{reaction}]{\text{HAT}} Fe^{n-1}{-}O{-}H + C\cdot$$

$$\Delta H^{O} = H^{O}_{FeO-H} - H^{O}_{FeO} + H^{O}_{C\bullet} - H^{O}_{C-H} \quad (1)$$

()

$$\Delta H^{O} = BDE_{C-H} - BDE_{FeO-H} \quad (2)$$

()

BDE's for nonheme $Fe^{III}O-H$ complexes with neutral N-rich ligands have been estimated to be between 78−87 kcal·mol^{-1},[67,68] and therefore, the BDE for the $Fe^{IV}O-H$ should be around 100 kcal·mol^{-1}. This number falls between the 103 kcal·mol^{-1} value estimated for the heme-thiolate peroxygenase Cpd I[27] and the 95 kcal·mol^{-1} value recently determined by a combination of experimental and theoretical methods in horseradish peroxidase and in an aromatic peroxidase as reported by Green and co-workers.[69] The $Fe^{IV}O-H$ value estimated for the present nonheme system constitutes one of the strongest described so far, attesting for the extraordinarily high HAT reactivity of **3**. Remarkably, this estimation of the BDE for the $Fe^{IV}O-H$ bond is in line with the value that we previously estimated on the basis of the reactivity of **3** toward toluene (estimated BDE_{O-H} = 101 kcal·mol^{-1}).[22] Interestingly, the ∼20 kcal·mol^{-1} difference in FeO−H strength between **2b** and **3** parallels the difference between the $Fe^{IV}O-H$ strength of Cpd I and $Fe^{III}O-H$ in Cpd II from an aromatic peroxidase described by Groves.[27] Instead, Green has deduced a reduced impact of oxidation state in FeO−H bond dissociation energies in a P450 mutant (CYP158) by a combination of red-ox titrations and theoretical methods; values of 95 and 90 kcal mol^{-1} for the $Fe^{IV}O-H$ and $Fe^{III}O-H$ bonds, respectively, were determined.[69]

The different nature of the sixth ligand in **2b** (CH_3CN) and **3** (carboxylate anion) deserves some comment. Acetonitrile is a neutral, π-acceptor ligand and stabilizes low oxidation states. On the other hand, acetate is an anionic sigma donor ligand that should favor higher oxidation states. Therefore, the extraordinarily higher reactivity of **3** when compared with **2b** is likely to be even tamed by the different ligand. In other words, if the two complexes would share exactly the same ligand set, differences in reaction rates are expected to be even larger.

It is also remarkable that the hydrogen-atom abstraction reactions carried out by **2** and **3** entail changes in the spin state along the reaction. HAT reactions from **3** (which has a S = 1/2 ground state) form an iron(IV)-hydroxo species, which possesses a S = 1 or S = 2 spin state, together with an alkyl radical. After the hydroxyl ligand rebound, an iron(III) complex with a S = 5/2 is formed concomitantly with the hydroxylated product. Thus, a change in the spin state occurs along this reaction path. Indeed, we and others have investigated the spin state changes along the reaction of oxoiron(V) with alkanes by computational methods[70,71] and disclosed that reactions usually occur at the S = 1/2 or S = 3/2 surfaces, depending on which of the two spin states has the lower energy barriers. In some instances, a spin crossover before reaching the first transition state is necessary to access the most energetically favored path. The S = 5/2 reaction path is usually much higher in energy with larger kinetic barriers. However, this is the most stable spin state for the reaction products, so that a spin crossover is necessary after the ligand rebound. A similar situation occurs with the HAT reactions carried out by oxoiron(IV) species analogous to **2**. In this case, most frequently reaction takes place at the quintuplet spin state (S = 2) even though the most stable spin configuration of the oxoiron(IV) is the triplet (S = 1).[72,73] (for a notable exception see ref 52. Thus, a spin crossover occurs before the transition state. In spite of the fact that spin-state changes are involved along the course of the reaction, spin−orbit couplings and spin−spin interactions remove the associated forbiddance. Thus, the feasibility of the HAT reactions carried out by oxoiron(IV) and oxoiron(V) species appears to be dictated by ground state thermodynamics rather than by multiple state reactivities.

Differences in Chemoselectivity between 2b and 3. The oxidation of cyclohexene constitutes a very informative mechanistic probe. Indeed, cyclohexene has been used as a substrate probe to study the reaction mechanism of oxidation reactions in enzymes and model systems.[74,75] This molecule provides the oxidant with two possible channels of reactivity: abstraction of an allylic C−H bond and OAT to the C=C bond. Analysis of the oxidized products formed upon reaction of **2b** or **3** with 100 equiv cyclohexene at −40 °C in CH_3CN showed completely different outcomes (Scheme 3). Under aerobic conditions, the oxoiron(IV) complex **2b** afforded mainly allylic oxidation (31% yield of allylic ketone and 5% yield of allylic alcohol with traces of epoxide), while the oxoiron(V) compound **3** afforded mainly cyclohexene oxide (60% yield) with minor amounts of allylic products (6% combined yield of allylic alcohol and ketone products). This comparison clearly indicates that **2b** is a sluggish OAT reagent

DOI: 10.1021/jacs.9b05758
J. Am. Chem. Soc. XXXX, XXX, XXX−XXX

Scheme 3. Product Distribution in the Reaction of 2b and 3 with Cyclohexene at −40 °C in CH_3CN under Aerobic Conditions

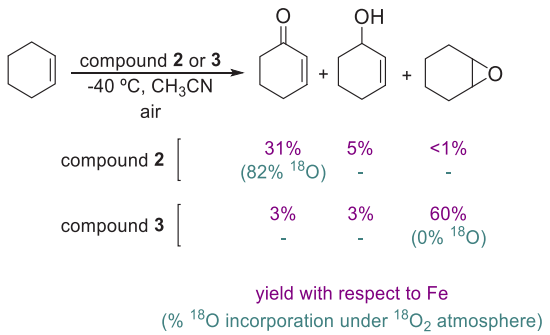

toward olefins, as previously observed for other oxoiron(IV) species,[75] and instead favors one-electron processes, such as hydrogen atom abstraction at the allylic position. In contrast, **3** is an excellent two-electron oxidant, epoxidizing C=C bonds instead of abstracting H atoms.

Interestingly, when these reactions were carried out under a $^{18}O_2$ atmosphere the allylic ketone product derived from the reaction of **2b** with cyclohexene incorporated 82% ^{18}O (Figure S25), which indicates that after hydrogen atom abstraction by **2b** the newly formed alkyl radical does not undergo rapid rebound and has a long enough lifetime to interact with gaseous dioxygen (Scheme 4). In contrast, no isotope labeling

Scheme 4. Hydrogen Atom Transfer from C−H Bonds by Oxoiron(IV) and Oxoiron(IV) Species

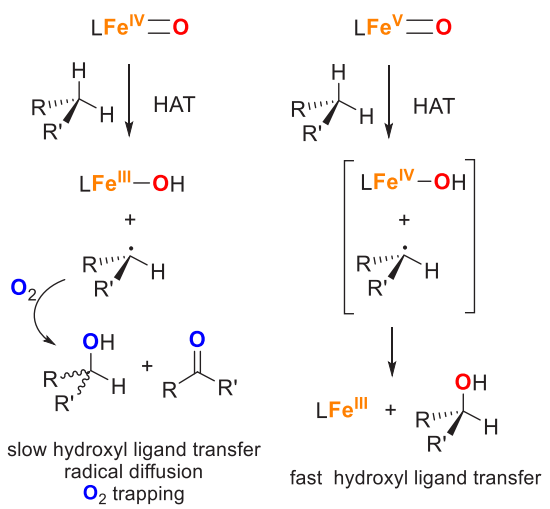

into the epoxide was detected in the same experiment carried out by **3** (Figure S25), which agrees with a direct OAT from the oxoiron(V) to the C=C bond. Of note, cyclohexene oxidation by **2b** under a N_2 atmosphere afforded the allylic alcohol as the major product (28% yield), while the production of allylic ketone was minimal (5% yield), which contrasts with the preferential formation of ketone in the presence of O_2. Finally, control experiments in the presence of triphenylphosphine have been done to exclude the formation of hydroperoxides under the different conditions tested (see Experimental Section).[76]

Differences in the Lifetime of the Carbon-Centered Radicals between 2b and 3. The outcome in the oxidation of cyclohexene with **2b** performed under $^{18}O_2$ atmosphere indicates that the hydroxyl ligand formed after HAT inefficiently rebounds with the newly formed carbon-centered radical, which diffuses out of the solvent cage, producing long-lived carbon-centered radicals that can interact with dioxygen, to give rise to the observed ^{18}O-labeling of the allylic ketone (Scheme 4). In striking contrast, **3** hydroxylates alkanes with stereoretention, as demonstrated by the hydroxylation of the tertiary C−H bonds of *cis*-1,2-dimethylcyclohexane by **3**, which occurs with 96% stereoretention.[22] This result excludes the formation of long-lived carbon-centered radicals and indicates that the formed alkyl radicals after HAT rapidly recombine with the hydroxyl bound to the iron(IV) with no time for stereoscrambling. To further demonstrate this idea, we have carried out the oxidation of cyclohexane with **3** under a $^{18}O_2$ atmosphere, which mainly affords cyclohexanol.[22] Conversely to what was observed in the oxidation of cyclohexene by **2b**, analysis of the cyclohexanol product showed no ^{18}O incorporation (Figure S26), further supporting the idea that the organic radicals formed along the reaction are very short-lived and do not have time to escape from the solvent cage and interact with atmospheric dioxygen.

Overall, the comparison between **2b** and **3** constitutes a unique case in nonheme systems providing convincing evidence that the lifetime of the carbon-centered radical formed after the initial hydrogen-atom transfer (HAT) is dependent on the oxidation state of the iron center (Scheme 4). The data indicates that the putative hydroxoiron(IV) intermediate, formed after initial HAT by the oxoiron(V) species **3**, can rapidly transfer the hydroxyl ligand (oxygen rebound) to the carbon-centered radical at reaction rates that exceed diffusion rates (10^9 s^{-1}). This observation is in line with the short lifetime of carbon-centered radicals formed by the heme enzyme cytochrome P450 (rate ~10^{10} to 10^{11} s^{-1}).[77] On the other hand, the reaction of the hydroxoiron(III) species, formed after HAT by the oxoiron(IV) species **2b**, with the carbon-centered radical is slower than diffusion out of the reaction pocket, so that the latter process dominates the outcome. Again, this observation finds wide precedent in previous studies on the C−H oxidation activity of nonheme oxoiron complexes[78] and in more recent reports in which the rebound rates of ferric-methoxide and ferric-hydroxide complexes with carbon-centered radicals have been directly measured.[79,80] The origin of this dichotomy may be tentatively traced to the redox nature of the rebound step, which entails a one-electron reduction of the iron center.

■ CONCLUSIONS

In this work we have described the synthesis and characterization of an oxoiron(IV) species with a neutral tetradentate N-based ligand, $[Fe^{IV}(O)(PyNMe_3)(CH_3CN)]^{2+}$, that according to our spectroscopic studies exists as a mixture of two isomers (**2a** and **2b**). The reactivity of the thermodynamically more stable isomer (**2b**) toward C−H bonds has been directly compared to that exhibited by the previously reported $1e^-$ oxidized species $[Fe^V(O)(OAc)(PyNMe_3)]^{2+}$ (**3**).[22] Our data show that the oxoiron(IV) species **2b** is 4 to 5 orders of magnitude slower than **3** in hydrogen atom abstraction reactions from C−H bonds. Analysis of the collected kinetic data indicates that the origin of this huge difference lies in the strength of the O−H bond formed after hydrogen-atom abstraction by the oxoiron unit and we estimate that the O−H bond formed upon reaction of **3** with a C−H bond is about 20

DOI: 10.1021/jacs.9b05758
J. Am. Chem. Soc. XXXX, XXX, XXX−XXX

kcal·mol^{-1} stronger than that derived from **2b**. On the basis of literature reports on the energy of the $Fe^{III}O-H$ bond of similar complexes, we estimate that the value of the $Fe^{IV}O-H$ bond derived from **3** is around 100 kcal·mol^{-1}, which is close to the reported values for highly active synthetic models of compound I of cytochrome P450. Overall, we have made a direct comparison between the oxidizing abilities of two nonheme oxoiron species with relevance in synthetic catalytic oxidation reactions, and we have established that the strength of the O−H bond formed after hydrogen atom abstraction is the key factor that determines their dramatic difference in HAT reactivity. In addition, our comparative study provides direct experimental evidence that the outcome of the carbon centered radical that forms after the initial HAT by the high valent oxo-iron complex is sensitive to the oxidation state of the complex. While **3** generates caged, short-lived radicals, **2** generates carbon-centered radicals that freely diffuse in solution. The most obvious consequence is that only **3** engages in stereoretentive hydroxylation reactions. Thus, the oxidation state of the iron center not only modulates the rate of HAT but also the rate of ligand rebound.

■ EXPERIMENTAL SECTION

Materials. Reagents and solvents used were of commercially available reagent quality unless otherwise stated. Solvents were purchased from Scharlab, Acros or Sigma-Aldrich and used without further purification. Preparation and handling of air-sensitive materials were carried out in an N_2 drybox (Jacomex) with O_2 and H_2O concentrations <1 ppm. $PyNMe_3$, $[Fe^{II}(CF_3SO_3)_2(PyNMe_3)]$ (**1·CF$_3$SO$_3$**) and **3** were prepared following previously described procedures.[22,81] $[Fe^{II}(PyNMe_3)(CH_3CN)_2]^{2+}$ (**1**) is obtained by exchange of the CF_3SO_3 anions by CH_3CN upon dissolving **1·CF$_3$SO$_3$** in this solvent. Xanthene-d_2 (>99% D enrichment) and 9,10-dihydroanthracene-d_4 (98% D enrichment) were prepared according to literature protocols.[82,83]

Physical Methods. UV−vis absorption spectroscopy was performed with an Agilent 50 Scan (Varian) UV−vis spectrophotometer with 1 cm quartz cells. Low temperature control was achieved with a cryostat from Unisoku Scientific Instruments, Japan. GC product analyses were performed on an Agilent 7820A gas chromatograph equipped with a HP-5 capillary column 30m × 0.32 mm × 0.25 mm and a flame ionization detector. GC−MS analyses were performed on an Agilent 7890A gas chromatograph equipped with an HP-5 capillary column interfaced with an Agilent 5975C mass spectrometer. For electron ionization (EI) the source was set at 70 eV, while a 50/50 NH_3:CH_4 mix was used as the ionization gas for chemical ionization (CI) analyses. High resolution mass spectra (HRMS) were recorded on a Bruker MicrOTOF-Q IITM instrument using ESI or Cryospray ionization sources at Serveis Tècnics of the University of Girona. Samples were introduced into the mass spectrometer ion source by direct infusion using a syringe pump and were externally calibrated using sodium triflate. The instrument was operated in positive ion mode.

Fe K-edge X-ray absorption spectra on the frozen solution of **2a** and **2b** were collected at 10 K in the energy range 6900 to 8000 eV on beamline 9−3 of the Stanford Synchrotron Radiation Lightsource (SSRL) of SLAC National Accelerator Laboratory. A 100-element solid-state Ge detectors (Canberra) were used to obtain the XAS data. An iron foil was used for the energy calibration of the beam and the first inflection point of the edge was assigned to 7112.0 eV. Seven scans of the fluorescence mode XAS spectra were collected on **2a** and **2b**. To increase the signal-to-noise ratio of the spectra, a 6-μm Mn filter along with the Soller slit was placed in between detector and the sample. Data reduction, averaging, and normalization were performed using the program EXAFSPAK.[84] The pre-edge features were fitted using the Fityk software[85] with pseudo-Voigt functions composed of 50:50 Gaussian/Lorentzian functions.

Resonance Raman spectra were obtained on frozen samples of **2a** and **2b** at 77 K with excitation at 457 nm laser (50 mW at source, Cobolt Lasers) through the sample in an NMR tube using a 135° scattering arrangement (parallel to the slit direction). The collimated Raman scattering was collected using two Plano convex lenses (f = 10 cm, placed at an appropriate distance) through appropriate long pass edge filters (Semrock) into an Acton AM-506M3 monochromator equipped with a Princeton Instruments ACTON PyLON LN/CCD-1340 × 400 detector. The detector was cooled to −120 °C prior to the experiments. Spectral calibration was performed using the Raman spectrum of acetonitrile/toluene 50:50 (v:v).[86] Each spectrum was accumulated, typically 60 times with 5 s acquisition time, resulting in a total acquisition time of 5 min per spectrum. The collected data was processed using Spectragryph,[87] and a multipoint baseline correction was performed for all spectra.

NMR spectra were recorded on a Bruker Avance III HD nanobay 400 MHz spectrometer or on a Bruker Ultrashield Avance III400. Temperatures for low temperature experiments were determined by calibration using a solution of methanol and TMS as the standard. 0.5 mL 4-mM solution of **1** was prepared for NMR experiments and the corresponding oxoiron(IV) samples were prepared by adding 1.1 equiv tBuNIO$_4$ and 1 equiv $HClO_4$ to this solution in an NMR tube at 253 K.

Mössbauer spectra were recorded with two spectrometers using Janis Research (Wilmington, MA) SuperVaritempdewars that allow studies in applied magnetic fields up to 7.5 T in the temperature range from 1.5 to 200 K. Mössbauer spectral simulations were performed using the WMOSS software package (SEE Co, Edina,MN). The figures of Mössbauer spectra were plotted in SpinCount (provided by Prof. M. P. Hendrich of Carnegie Mellon University).

Synthesis of $[Fe^{II}(PyNMe_3)(CH_3CN)_2](SbF_6)_2$ (1·SbF$_6$). In the glovebox, $PyNMe_3$ (41.3 mg, 0.17 mmol) was dissolved in CH_3CN (2 mL). Afterward $FeCl_2$ (21.1 mg, 0.17 mmol) was added directly as a solid and the mixture was stirred for 24 h. A color change from pale yellow to deep orange was observed. Then, $AgSbF_6$ (121 mg, 0.34 mmol) was added, which caused the immediate formation of a white precipitate corresponding to AgCl and the solution turned dark green. After stirring for 2 h the solution was filtered over Celite to remove precipitated AgCl. Then, direct addition of diethyl ether (10 mL) caused the precipitation of the complex which was separated and dried. Finally, the resulting solid was dissolved using a mixture of CH_2Cl_2 (1.5 mL) and CH_3CN (0.5 mL). Slow diethyl ether diffusion over the resulting solution in the anaerobic box afforded 41.8 mg (0.05 mmol, 32% yield) of dark brown crystals corresponding to **1·SbF$_6$** suitable for X-ray diffraction (see SI). ^{1}H NMR (CD_3CN, 400 MHz, 298 K) δ, ppm 114, 99, 87, 77, 66, 56, 55, 12, −24, −35. ESI-QTOF-MS (m/z) calcd for $[Fe(PyNMe_3)(CH_3CN)]^{2+}$172.5802, found 172.5806; calcd for $[Fe(PyNMe_3)](SbF_6)]^+$ 539.0287, found 539.0290. Anal. Calcd for $C_{18}H_{30}F_{12}FeN_6Sb_2$: C, 25.20; H, 3.53; N: 9.80. Found: C, 25.18; H, 3.21; N, 9.72.

Synthesis of PyNMe$_3$-d_4. $PyNMe_3$ (96.6 mg, 0.39 mmol) and NaH (39.3 mg, 1.56 mmol) were suspended in CD_3CN (2.5 mL) in a two-necked round flask inside the glovebox. The mixture was taken out the glovebox and stirred at 50 °C under an inert atmosphere for 24 h. Then D_2O (2 mL) was added to quench the reaction. Upon removal of CD_3CN under vacuum, the residue was extracted with CH_2Cl_2 (4 × 10 mL) and the organic layer was dried with $MgSO_4$ and filtered. The solvent was removed under reduced pressure obtaining a brown oil. The product was further purified by column chromatography over silica using an initial mixture of CH_2Cl_2:MeOH:NH_3 80:20:4 and slowly raising the polarity to 60:40:4 to ensure the complete elution of PyNMe$_3$-d_4. 53.2 mg (0.21 mmol, 54% yield) of the pure deuterated ligand were obtained. ^{1}H NMR ($CDCl_3$, 400 MHz, 298 K) δ, ppm 7.58 (t, J = 7.7 Hz, 1H), 7.10 (d, J = 7.7 Hz, 2H), 2.55−2.46 (m, 14H), 2.21 (s, 3H). ^{13}C NMR ($CDCl_3$, 100 MHz, 298 K) δ, ppm 157.4, 136.8, 122.2, 61.9 (m), 53.1, 52.4, 45.1 (2C).

Synthesis of $[Fe^{II}(CF_3SO_3)_2(PyNMe_3\text{-}d_4)]$ (1·CF$_3$SO$_3$-d_4). $[Fe^{II}(CF_3SO_3)_2(CH_3CN)_2]$ (91.9 mg, 0.21 mmol) was added directly as a solid to a vigorously stirred solution of PyNMe$_3$-d_4 (53.2 mg, 0.21

DOI: 10.1021/jacs.9b05758
J. Am. Chem. Soc. XXXX, XXX, XXX−XXX

mmol) in tetrahydrofuran (2 mL). The solution turned from a pale color to an intense yellow color. The mixture was stirred overnight and then the obtained precipitate was separated, washed with tetrahydrofuran and dried under vacuum. Finally, the solid was redissolved in the minimum amount of CH_2Cl_2 and a few drops of acetonitrile were added to ensure the complete dissolution of the complex. After filtration over Celite, slow diethyl ether diffusion over the resulting solution afforded 63.9 mg (0.11 mmol, 52%) of yellow crystals. ^{1}H NMR (CD_3CN, 243 MHz, 298 K) δ, ppm = 44.8, 34.1, 24.5, 18.7, 10.5, −10.7. ESI-QTOF-MS (m/z) calcd for $[Fe(PyNMe_3\text{-}d_4)(OH_2)]^{2+}$ 163.0848, found 163.0856; calcd for $[Fe(PyNMe_3\text{-}d_4)](OTf)]^+$ 457.1116, found 457.1125.

Generation of 2 with Bu_4NIO_4 and TfOH. A 1 mM solution of **1** in CH_3CN (or in a 1:1 mixture of CH_3CN:CH_2Cl_2) was prepared into the glovebox. Two mL of this solution (2 μmol of **1**) were introduced in a UV−vis cuvette, that was capped with a septum, taken out from the glovebox, placed in the cryostat of the UV−vis spectrophotometer and cooled down to the set temperature (−20, −40, or −60 °C). Once the desired temperature was reached, an initial UV−vis absorption spectrum of **1** was recorded. Then 60 μL of a solution containing 1.1 equiv Bu_4NIO_4 and 0.8 equiv TfOH in CH_3CN were added in the cuvette. The formation of two bands at ∼800 and ∼980 nm was immediately observed. When the generation of **2** was carried out at −20 °C, the band at ∼980 nm (**2b**) was the most intense. Conversely, at −60 °C the band at ∼800 nm was the highest in intensity (corresponding to a mixture of **2a** and **2b**). Finally, at −40 °C the band at ∼800 nm was the most intense right after addition of the oxidant (mixture of **2a** and **2b**) but it decreased over time in favor of the one at ∼980 nm (**2b**) that became the major one.

The oxoiron(IV) complexes **2b**-d_4 and **2·SbF$_6$** were generated following the above-described method for the preparation of **2** but using **1·CF$_3$SO$_3$**-d_4 or **1·SbF$_6$** as starting material.

Generation of 2 with 2-*t*BuSO$_2$−C$_6$H$_4$IO. A 1 mM solution of **1** in CH_3CN was prepared into the glovebox. Two mL of this solution (2 μmol of **1**) were introduced in a UV−vis cuvette that was capped with a septum, taken out from the glovebox, placed in the cryostat of the UV−vis spectrophotometer and cooled down to −40 °C. Once the desired temperature was reached, an initial UV−vis absorption spectrum of **1** was recorded. Then 100 μL of a solution containing 2-*t*BuSO$_2$−C$_6$H$_4$IO (2.2 μmol) in CH_2Cl_2 were added in the cuvette. As previously observed in the generation of **2** with 1.1 equiv Bu_4NIO_4 and 0.8 equiv TfOH, the intensity of the band at ∼800 nm decreased over time in favor of the one at ∼980 nm, which became the most intense.

Reaction of 2 with Substrates. For the reactivity studies, **2** was generated as described above using Bu_4NIO_4 and TfOH.

*Oxidation of p-X-thioanisole by **2b** at −40 °C.* Once **2b** was fully formed in CH_3CN, 50 or 100 μL of a solution of the substrate in CH_3CN containing the desired amount of substrate (10−100 equiv) were added. The characteristic absorption band at 990 nm of **2b** decayed following a single exponential function from which kinetic data could be extracted. In the case of thioanisole, after total decay of the UV−vis absorption band of **2b**, biphenyl was added as internal standard and the reaction mixture was rapidly filtered through a silica plug, which was washed with ethyl acetate. This solution was then analyzed with GC to calculate the product yield.

*Oxidation of Hydrocarbons by **2b** at −40 °C.* Once **2b** was fully formed in a 1:1 mixture of CH_3CN:CH_2Cl_2, between 100 and 250 μL of a solution containing the desired amount of substrate (10−70 equiv) in a 1:1 mixture of CH_3CN:CH_2Cl_2 were added. The characteristic absorption band at 990 nm of **2b** decayed following a single exponential function from which kinetic data could be extracted.

*Oxidation of Sulfides and Hydrocarbons by **2a** at −60 °C in a 1:1 Mixture of CH_3CN:CH_2Cl_2.* To a solution of compound **2a** + **2b**, generated in a 1:1 mixture of CH_3CN:CH_2Cl_2 at −60 °C (see above for more details), 100 μL of a solution containing the desired amount of substrate (10−46 equiv) in a 1:1 mixture of CH_3CN:CH_2Cl_2 were added. Disappearance of the UV−vis absorption band at 792 nm was monitored upon substrate addition and the decay was fitted to a single exponential after subtraction of the contribution from **2b** (see Supporting Information for more details)

*Oxidation of Sulfides and Hydrocarbons with **2b** at −60 °C in a 1:1 Mixture of CH_3CN:CH_2Cl_2.* A solution of **2b** was obtained at −40 °C in a 1:1 mixture of CH_3CN:CH_2Cl_2 (see above for more details) after isomerization of **2a**. The solution of **2b** was cooled down to -60 °C and 100 μL of a solution containing the desired amount of substrate (10−46 equiv) in a 1:1 mixture of CH_3CN:CH_2Cl_2 were added. Disappearance of the UV−vis absorption band characteristic of **2b** at 990 nm was monitored upon substrate addition and the decay was fitted to a single exponential function from which the reaction rate could be extracted.

*Oxidation of Cyclohexene with **2b** and **3** at −40 °C.* Once **2b** or **3** were fully formed in pure CH_3CN, 200 μL of a solution containing 100 equiv of cyclohexene in CH_3CN were added. After total decay of the UV−vis absorption band of **2b** at 990 nm or **3** at 490 nm, biphenyl was added as internal standard and the reaction mixture was rapidly filtered through a silica plug and subsequently washed with ethyl acetate. At this point an aliquot of the solution was analyzed by GC and GC−MS. To the remaining solution, an excess of solid PPh_3 was added and analyzed by GC to exclude the formation of hydroperoxides, as previously reported.[76] This experiment was carried out under different atmospheres, namely N_2, air and $^{18}O_2$.

*Oxidation of Cyclohexane by **3** at −40 °C.* Once **3** was fully formed in CH_3CN, 100 μL of a solution containing 45 equiv of cyclohexane in CH_3CN were added. After total decay of the UV−vis absorption band of **3** at 490 nm, the reaction mixture was rapidly filtered through a silica plug and subsequently washed with ethyl acetate. At this point an aliquot of the solution was analyzed by GC and GC−MS. This experiment was carried out under N_2 and $^{18}O_2$ atmospheres.

*Eyring Plot for the Reaction of **2b** with Cyclohexadiene and Xanthene.* Once **2b** was fully formed in a 1:1 mixture of CH_3CN:CH_2Cl_2, 100 μL of a solution containing 10 equiv of cyclohexadiene or xanthene in a 1:1 mixture of CH_3CN:CH_2Cl_2 were added. The decay of the absorption band of **2b** at 990 nm was monitored and fitted to a single exponential function from which the observed rate constant (k_{obs}) could be extracted. This experiment was repeated at five different temperatures (233−273 K) for each substrate, in order to calculate the activation parameters ($\Delta H^{\ddagger}$ and $\Delta S^{\ddagger}$) by plotting the $\ln(k_2/T)$ values as a function of $1/T$.

■ ASSOCIATED CONTENT

Supporting Information

The Supporting Information is available free of charge on the ACS Publications website at DOI: 10.1021/jacs.9b05758.

Characterization of **PyNMe$_3$**-d_4, **1·CF$_3$SO$_3$**-d_4, and **1·SbF$_6$**, XAS analysis for **2a** and **2b**, raw Mössbauer spectra for **2a** and **2b**, ^{1}H NMR characterization of **2b** and **2b**-d_4, UV−vis spectroscopy of the conversion of **2a** to **2b** and comparison of their reactivities in OAT and HAT processes, UV−vis spectroscopy of the reaction of **2b** in OAT and HAT processes, MS spectra for the reactions of **2b** and **3** with cyclohexene and cyclohexane, DFT calculations for the structure of **2a** and **2b** including predicted ^{1}H NMR chemical shifts and geometry coordinates (PDF)

Crystal data (CIF)

■ AUTHOR INFORMATION

Corresponding Authors

*E-mail: larryque@umn.edu.

*E-mail: miquel.costas@udg.edu.

*E-mail: anna.company@udg.edu.

DOI: 10.1021/jacs.9b05758
J. Am. Chem. Soc. XXXX, XXX, XXX−XXX

ORCID

Valeria Dantignana: 0000-0002-0799-5800
Joan Serrano-Plana: 0000-0003-2735-0943
Apparao Draksharapu: 0000-0001-7897-3230
Saikat Banerjee: 0000-0003-0013-8037
Ruixi Fan: 0000-0002-6996-4276
Ilaria Gamba: 0000-0001-9136-7227
Yisong Guo: 0000-0002-4132-3565
Lawrence Que, Jr.: 0000-0002-0989-2813
Miquel Costas: 0000-0001-6326-8299
Anna Company: 0000-0003-4845-4418

Present Addresses

[‖]J. Serrano-Plana: Department of Chemistry, University of Basel, Mattenstrasse 24a, BPR 1096, Switzerland.
[⊥]A. Draksharapu: SL-208A, Department of Chemistry, Indian Institute of Technology Kanpur, Kanpur 208016, India.

Notes

The authors declare no competing financial interest.

■ ACKNOWLEDGMENTS

The work at the University de Girona was supported by the Spanish Ministry of Science (CTQ2015-70795-P to M.C., CTQ2016-77989-P to A.C.) and Generalitat de Catalunya (ICREA Academia Award to M.C. and 2014 SGR 862). The European Commission is acknowledged for financial support through the NoNoMeCat project (675020-MSCA-ITN-2015-ETN). The work at the University of Minnesota and Carnegie Mellon University was supported by the US National Science Foundation respectively through grants CHE-1665391 to L.Q. and CHE-1654060 to Y.G.). XAS data were collected on Beamline 9-3 at the Stanford Synchrotron Radiation Light source, SLAC National Accelerator Laboratory. SLAC is supported by the U.S. Department of Energy (DOE), Office of Science, Office of Basic Energy Sciences under Contract No. DE-AC02-76SF00515. Use of Beamline 9-3 is supported by the DOE Office of Biological and Environmental Research and the National Institutes of Health, National Institute of General Medical Sciences (including P41GM103393). The Bruker Avance III HD nanobay 400 MHz spectrometer used in this study was purchased from funds provided by the Office of the Vice President of Research, the College of Science and Engineering, and the Department of Chemistry at the University of Minnesota. We thank the Pittsburgh Supercomputing Center for granting us computational resources (CHE180020P to R.F. and Y.G.).

■ REFERENCES

(1) Rittle, J.; Green, M. T. Cytochrome P450 Compound I: Capture, Characterization, and C-H Bond Activation Kinetics. *Science* **2010**, *330*, 933−937.

(2) Huang, X.; Groves, J. T. Oxygen Activation and Radical Transformations in Heme Proteins and Metalloporphyrins. *Chem. Rev.* **2018**, *118*, 2491−2553.

(3) Ortiz de Montellano, P. R. Hydrocarbon Hydroxylation by Cytochrome P450 Enzymes. *Chem. Rev.* **2010**, *110*, 932−948.

(4) Shaik, S.; Cohen, S.; Wang, Y.; Chen, H.; Kumar, D.; Thiel, W. P450 Enzymes: Their Structure, Reactivity, and Selectivity-Modeled by QM/MM Calculations. *Chem. Rev.* **2010**, *110*, 949−1017.

(5) Perry, C.; de los Santos; Emmanuel, L. C.; Alkhalaf, L. M.; Challis, G. L. Rieske non-heme iron-dependent oxygenases catalyse diverse reactions in natural product biosynthesis. *Nat. Prod. Rep.* **2018**, *35*, 622−632.

(6) Kovaleva, E. G.; Lipscomb, J. D. Versatility of biological non-heme Fe(II) centers in oxygen activation reactions. *Nat. Chem. Biol.* **2008**, *4*, 186.

(7) Chakrabarty, S.; Austin, R. N.; Deng, D.; Groves, J. T.; Lipscomb, J. D. Radical Intermediates in Monooxygenase Reactions of Rieske Dioxygenases. *J. Am. Chem. Soc.* **2007**, *129*, 3514−3515.

(8) Krebs, C.; Galonić Fujimori, D.; Walsh, C. T.; Bollinger, J. M. Non-Heme Fe(IV)−Oxo Intermediates. *Acc. Chem. Res.* **2007**, *40*, 484−492.

(9) Price, J. C.; Barr, E. W.; Tirupati, B.; Bollinger, J. M.; Krebs, C. The First Direct Characterization of a High-Valent Iron Intermediate in the Reaction of an α-Ketoglutarate-Dependent Dioxygenase: A High-Spin Fe(IV) Complex in Taurine/α-Ketoglutarate Dioxygenase (TauD) from Escherichia coli. *Biochemistry* **2003**, *42*, 7497−7508.

(10) Hoffart, L. M.; Barr, E. W.; Guyer, R. B.; Bollinger, J. M.; Krebs, C. Direct spectroscopic detection of a C-H-cleaving high-spin Fe(IV) complex in a prolyl-4-hydroxylase. *Proc. Natl. Acad. Sci. U. S. A.* **2006**, *103*, 14738−14743.

(11) Eser, B. E.; Barr, E. W.; Frantom, P. A.; Saleh, L.; Bollinger, J. M.; Krebs, C.; Fitzpatrick, P. F. Direct Spectroscopic Evidence for a High-Spin Fe(IV) Intermediate in Tyrosine Hydroxylase. *J. Am. Chem. Soc.* **2007**, *129*, 11334−11335.

(12) Panay, A. J.; Lee, M.; Krebs, C.; Bollinger, J. M.; Fitzpatrick, P. F. Evidence for a High-Spin Fe(IV) Species in the Catalytic Cycle of a Bacterial Phenylalanine Hydroxylase. *Biochemistry* **2011**, *50*, 1928−1933.

(13) Wong, S. D.; Srnec, M.; Matthews, M. L.; Liu, L. V.; Kwak, Y.; Park, K.; Bell, C. B., III; Alp, E. E.; Zhao, J.; Yoda, Y.; Kitao, S.; Seto, M.; Krebs, C.; Bollinger, J. M.; Solomon, E. I. Elucidation of the Fe(IV)═O intermediate in the catalytic cycle of the halogenase SyrB2. *Nature* **2013**, *499*, 320.

(14) Galonić Fujimori, D.; Barr, E. W.; Matthews, M. L.; Koch, G. M.; Yonce, J. R.; Walsh, C. T.; Bollinger, J. M.; Krebs, C.; Riggs-Gelasco, P. J. Spectroscopic Evidence for a High-Spin Br-Fe(IV)-Oxo Intermediate in the α-Ketoglutarate-Dependent Halogenase CytC3 from Streptomyces. *J. Am. Chem. Soc.* **2007**, *129*, 13408−13409.

(15) Galonić, D. P.; Barr, E. W.; Walsh, C. T.; Bollinger, J. M., Jr; Krebs, C. Two interconverting Fe(IV) intermediates in aliphatic chlorination by the halogenase CytC3. *Nat. Chem. Biol.* **2007**, *3*, 113.

(16) McDonald, A. R.; Que, L. High-valent nonheme iron-oxo complexes: Synthesis, structure, and spectroscopy. *Coord. Chem. Rev.* **2013**, *257*, 414−428.

(17) Ray, K.; Pfaff, F. F.; Wang, B.; Nam, W. Status of Reactive Non-Heme Metal−Oxygen Intermediates in Chemical and Enzymatic Reactions. *J. Am. Chem. Soc.* **2014**, *136*, 13942−13958.

(18) Guo, M.; Corona, T.; Ray, K.; Nam, W. Heme and Nonheme High-Valent Iron and Manganese Oxo Cores in Biological and Abiological Oxidation Reactions. *ACS Cent. Sci.* **2019**, *5*, 13−28.

(19) Oloo, W. N.; Que, L. Bioinspired Nonheme Iron Catalysts for C−H and C═C Bond Oxidation: Insights into the Nature of the Metal-Based Oxidants. *Acc. Chem. Res.* **2015**, *48*, 2612−2621.

(20) Olivo, G.; Cussó, O.; Borrell, M.; Costas, M. Oxidation of alkane and alkene moieties with biologically inspired nonheme iron catalysts and hydrogen peroxide: from free radicals to stereoselective transformations. *JBIC, J. Biol. Inorg. Chem.* **2017**, *22*, 425−452.

(21) Meyer, S.; Klawitter, I.; Demeshko, S.; Bill, E.; Meyer, F. A Tetracarbene−Oxoiron(IV) Complex. *Angew. Chem., Int. Ed.* **2013**, *52*, 901−905.

(22) Serrano-Plana, J.; Oloo, W. N.; Acosta-Rueda, L.; Meier, K. K.; Verdejo, B.; García-España, E.; Basallote, M. G.; Münck, E.; Que, L.; Company, A.; Costas, M. Trapping a Highly Reactive Nonheme Iron Intermediate That Oxygenates Strong C-H Bonds with Stereo-retention. *J. Am. Chem. Soc.* **2015**, *137*, 15833−15842.

(23) de Oliveira, F. T.; Chanda, A.; Banerjee, D.; Shan, X.; Mondal, S.; Que, L.; Bominaar, E. L.; Münck, E.; Collins, T. J. Chemical and Spectroscopic Evidence for an Fe^{V}-Oxo Complex. *Science* **2007**, *315*, 835−838.

DOI: 10.1021/jacs.9b05758
J. Am. Chem. Soc. XXXX, XXX, XXX−XXX

(24) Kwon, E.; Cho, K.-B.; Hong, S.; Nam, W. Mechanistic insight into the hydroxylation of alkanes by a nonheme iron(V)−oxo complex. *Chem. Commun.* **2014**, *50*, 5572−5575.

(25) Ghosh, M.; Singh, K. K.; Panda, C.; Weitz, A.; Hendrich, M. P.; Collins, T. J.; Dhar, B. B.; Sen Gupta, S. Formation of a Room Temperature Stable $Fe^{V}(O)$ Complex: Reactivity Toward Unactivated C−H Bonds. *J. Am. Chem. Soc.* **2014**, *136*, 9524−9527.

(26) Collins, T. J.; Ryabov, A. D. Targeting of High-Valent Iron-TAML Activators at Hydrocarbons and Beyond. *Chem. Rev.* **2017**, *117*, 9140−9162.

(27) Wang, X.; Peter, S.; Kinne, M.; Hofrichter, M.; Groves, J. T. Detection and Kinetic Characterization of a Highly Reactive Heme−Thiolate Peroxygenase Compound I. *J. Am. Chem. Soc.* **2012**, *134*, 12897−12900.

(28) Fan, R.; Serrano-Plana, J.; Oloo, W. N.; Draksharapu, A.; Delgado-Pinar, E.; Company, A.; Martin-Diaconescu, V.; Borrell, M.; Lloret-Fillol, J.; García-España, E.; Guo, Y.; Bominaar, E. L.; Que, L.; Costas, M.; Münck, E. Spectroscopic and DFT Characterization of a Highly Reactive Nonheme Fe^{V}−Oxo Intermediate. *J. Am. Chem. Soc.* **2018**, *140*, 3916−3928.

(29) Mondal, B.; Neese, F.; Bill, E.; Ye, S. Electronic Structure Contributions of Non-Heme Oxo-Iron(V) Complexes to the Reactivity. *J. Am. Chem. Soc.* **2018**, *140*, 9531−9544.

(30) Lyakin, O. Y.; Zima, A. M.; Samsonenko, D. G.; Bryliakov, K. P.; Talsi, E. P. EPR Spectroscopic Detection of the Elusive Fe^{V}═O Intermediates in Selective Catalytic Oxofunctionalizations of Hydrocarbons Mediated by Biomimetic Ferric Complexes. *ACS Catal.* **2015**, *5*, 2702−2707.

(31) Zima, A. M.; Lyakin, O. Y.; Ottenbacher, R. V.; Bryliakov, K. P.; Talsi, E. P. Dramatic Effect of Carboxylic Acid on the Electronic Structure of the Active Species in Fe(PDP)-Catalyzed Asymmetric Epoxidation. *ACS Catal.* **2016**, *6*, 5399−5404.

(32) Zima, A. M.; Lyakin, O. Y.; Ottenbacher, R. V.; Bryliakov, K. P.; Talsi, E. P. Iron-Catalyzed Enantioselective Epoxidations with Various Oxidants: Evidence for Different Active Species and Epoxidation Mechanisms. *ACS Catal.* **2017**, *7*, 60−69.

(33) Oloo, W. N.; Banerjee, R.; Lipscomb, J. D.; Que, L. Equilibrating $(L)Fe^{III}$−OOAc and $(L)Fe^{V}(O)$ Species in Hydrocarbon Oxidations by Bio-Inspired Nonheme Iron Catalysts Using H_2O_2 and AcOH. *J. Am. Chem. Soc.* **2017**, *139*, 17313−17326.

(34) White, M. C.; Zhao, J. Aliphatic C−H Oxidations for Late-Stage Functionalization. *J. Am. Chem. Soc.* **2018**, *140*, 13988−14009.

(35) Serrano-Plana, J.; Acuña-Parés, F.; Dantignana, V.; Oloo, W. N.; Castillo, E.; Draksharapu, A.; Whiteoak, C. J.; Martin-Diaconescu, V.; Basallote, M. G.; Luis, J. M.; Que, L.; Costas, M.; Company, A. Acid-Triggered O−O Bond Heterolysis of a Nonheme $Fe^{III}(OOH)$ Species for the Stereospecific Hydroxylation of Strong C−H Bonds. *Chem. - Eur. J.* **2018**, *24*, 5331−5340.

(36) Klein, J. E. M. N.; Que, L. Biomimetic High-Valent Mononuclear Nonheme Iron-Oxo Chemistry. In *Encyclopedia of Inorganic and Bioinorganic Chemistry*; Scott, R. A., Ed.; John Wiley & Sons, 2016; pp 1−22.

(37) Rasheed, W.; Draksharapu, A.; Banerjee, S.; Young, V. G., Jr.; Fan, R.; Guo, Y.; Ozerov, M.; Nehrkorn, J.; Krzystek, J.; Telser, J.; Que, L., Jr. Crystallographic Evidence for a Sterically Induced Ferryl Tilt in a Non-Heme Oxoiron(IV) Complex that Makes it a Better Oxidant. *Angew. Chem., Int. Ed.* **2018**, *57*, 9387−9391.

(38) Company, A.; Prat, I.; Frisch, J. R.; Mas-Ballesté, D. R.; Güell, M.; Juhász, G.; Ribas, X.; Münck, D. E.; Luis, J. M.; Que, L.; Costas, M. Modeling the cis-Oxo-Labile Binding Site Motif of Non-Heme Iron Oxygenases: Water Exchange and Oxidation Reactivity of a Non-Heme Iron(IV)-Oxo Compound Bearing a Tripodal Tetradentate Ligand. *Chem. - Eur. J.* **2011**, *17*, 1622−1634.

(39) Anastasi, A. E.; Comba, P.; McGrady, J.; Lienke, A.; Rohwer, H. Electronic Structure of Bispidine Iron(IV) Oxo Complexes. *Inorg. Chem.* **2007**, *46*, 6420−6426.

(40) Prakash, J.; Rohde, G. T.; Meier, K. K.; Münck, E.; Que, L. Upside Down! Crystallographic and Spectroscopic Characterization of an $[Fe^{IV}(O_{syn})(TMC)]^{2+}$ Complex. *Inorg. Chem.* **2015**, *54*, 11055−11057.

(41) Klinker, E. J.; Kaizer, J.; Brennessel, W. W.; Woodrum, N. L.; Cramer, C. J.; Que, L., Jr. Structures of Nonheme Oxoiron(IV) Complexes from X-ray Crystallography, NMR Spectroscopy, and DFT Calculations. *Angew. Chem., Int. Ed.* **2005**, *44*, 3690−3694.

(42) Company, A.; Sabenya, G.; González-Béjar, M.; Gómez, L.; Clémancey, M.; Blondin, G.; Jasniewski, A. J.; Puri, M.; Browne, W. R.; Latour, J.-M.; Que, L.; Costas, M.; Pérez-Prieto, J.; Lloret-Fillol, J. Triggering the Generation of an Iron(IV)-Oxo Compound and Its Reactivity toward Sulfides by RuII Photocatalysis. *J. Am. Chem. Soc.* **2014**, *136*, 4624−4633.

(43) Rasheed, W.; Fan, R.; Abelson, C. S.; Peterson, P. O.; Ching, W. M.; Guo, Y.; Que, L., Jr. Structural Implications of the Paramagnetically Shifted NMR Signals from Pyridine H-Atoms on Synthetic Nonheme Fe^{IV}═O Complexes. *JBIC, J. Biol. Inorg. Chem.* **2019**, *24*, 533−545.

(44) Ching, W.-M.; Zhou, A.; Klein, J. E. M. N.; Fan, R.; Knizia, G.; Cramer, C. J.; Guo, Y.; Que, L. Characterization of the Fleeting Hydroxoiron(III) Complex of the Pentadentate TMC-py Ligand. *Inorg. Chem.* **2017**, *56*, 11129−11140.

(45) Duban, E. A.; Bryliakov, K. P.; Talsi, E. P. The Active Intermediates of Non-Heme-Iron-Based Systems for Catalytic Alkene Epoxidation with H_2O_2/CH_3COOH. *Eur. J. Inorg. Chem.* **2007**, *2007*, 852−857.

(46) Thibon, A.; England, J.; Martinho, M.; Young, V. G., Jr.; Frisch, J. R.; Guillot, R.; Girerd, J.-J.; Münck, E.; Que, L., Jr.; Banse, F. Proton- and Reductant-Assisted Dioxygen Activation by a Nonheme Iron(II) Complex to Form an Oxoiron(IV) Intermediate. *Angew. Chem., Int. Ed.* **2008**, *47*, 7064−7067.

(47) Park, M. J.; Lee, J.; Suh, Y.; Kim, J.; Nam, W. Reactivities of Mononuclear Non-Heme Iron Intermediates Including Evidence that Iron(III)−Hydroperoxo Species Is a Sluggish Oxidant. *J. Am. Chem. Soc.* **2006**, *128*, 2630−2634.

(48) Notice that 9,10-dihydroanthracene-d_{14} could be synthesized with only a 98% D enrichment. If this is taken into account, a much higher KIE should have been obtained.

(49) Hong, S.; So, H.; Yoon, H.; Cho, K.-B.; Lee, Y.-M.; Fukuzumi, S.; Nam, W. Reactivity comparison of high-valent iron(IV)-oxo complexes bearing N-tetramethylated cyclam ligands with different ring size. *Dalton Trans.* **2013**, *42*, 7842−7845.

(50) Price, J. C.; Barr, E. W.; Glass, T. E.; Krebs, C.; Bollinger, J. M. Evidence for Hydrogen Abstraction from C1 of Taurine by the High-Spin Fe(IV) Intermediate Detected during Oxygen Activation by Taurine:α-Ketoglutarate Dioxygenase (TauD). *J. Am. Chem. Soc.* **2003**, *125*, 13008−13009.

(51) Bollinger, J. M.; Krebs, C. Stalking intermediates in oxygen activation by iron enzymes: Motivation and method. *J. Inorg. Biochem.* **2006**, *100*, 586−605.

(52) Kupper, C.; Mondal, B.; Serrano-Plana, J.; Klawitter, I.; Neese, F.; Costas, M.; Ye, S.; Meyer, F. Nonclassical Single-State Reactivity of an Oxo-Iron(IV) Complex Confined to Triplet Pathways. *J. Am. Chem. Soc.* **2017**, *139*, 8939−8949.

(53) Monte Pérez, I.; Engelmann, X.; Lee, Y.-M.; Yoo, M.; Kumaran, E.; Farquhar, E. R.; Bill, E.; England, J.; Nam, W.; Swart, M.; Ray, K. A Highly Reactive Oxoiron(IV) Complex Supported by a Bioinspired N_3O Macrocyclic Ligand. *Angew. Chem., Int. Ed.* **2017**, *56*, 14384−14388.

(54) Mitra, M.; Nimir, H.; Demeshko, S.; Bhat, S. S.; Malinkin, S. O.; Haukka, M.; Lloret-Fillol, J.; Lisensky, G. C.; Meyer, F.; Shteinman, A. A.; Browne, W. R.; Hrovat, D. A.; Richmond, M. G.; Costas, M.; Nordlander, E. Nonheme Fe(IV) Oxo Complexes of Two New Pentadentate Ligands and Their Hydrogen-Atom and Oxygen-Atom Transfer Reactions. *Inorg. Chem.* **2015**, *54*, 7152−7164.

(55) Kaizer, J.; Klinker, E. J.; Oh, N. Y.; Rohde, J.-U.; Song, W. J.; Stubna, A.; Kim, J.; Münck, E.; Nam, W.; Que, L. Nonheme $Fe^{IV}O$ Complexes That Can Oxidize the C−H Bonds of Cyclohexane at Room Temperature. *J. Am. Chem. Soc.* **2004**, *126*, 472−473.

DOI: 10.1021/jacs.9b05758
J. Am. Chem. Soc. XXXX, XXX, XXX−XXX

(56) Biswas, A. N.; Puri, M.; Meier, K. K.; Oloo, W. N.; Rohde, G. T.; Bominaar, E. L.; Münck, E.; Que, L. Modeling TauD-J: A High-Spin Nonheme Oxoiron(IV) Complex with High Reactivity toward C−H Bonds. *J. Am. Chem. Soc.* **2015**, *137*, 2428−2431.

(57) Tanko, J. M.; Friedline, F.; Suleman, N. K.; Castagnoli, N., Jr. tert-Butoxyl as a Model for Radicals in Biological Systems: Caveat Emptor. *J. Am. Chem. Soc.* **2001**, *123*, 5808−5809.

(58) Finn, M.; Friedline, R.; Suleman, N. K.; Wohl, C. J.; Tanko, J. M. Chemistry of the t-Butoxyl Radical: Evidence that Most Hydrogen Abstractions from Carbon are Entropy-Controlled. *J. Am. Chem. Soc.* **2004**, *126*, 7578−7584.

(59) Pattanayak, S.; Jasniewski, A. J.; Rana, A.; Draksharapu, A.; Singh, K. K.; Weitz, A.; Hendrich, M.; Que, L.; Dey, A.; Sen Gupta, S. Spectroscopic and Reactivity Comparisons of a Pair of bTAML Complexes with Fe^{V}═O and Fe^{IV}═O Units. *Inorg. Chem.* **2017**, *56*, 6352−6361.

(60) Oszajca, M.; Franke, A.; Drzewiecka-Matuszek, A.; Brindell, M.; Stochel, G.; van Eldik, R. Temperature and Pressure Effects on C−H Abstraction Reactions Involving Compound I and II Mimics in Aqueous Solution. *Inorg. Chem.* **2014**, *53*, 2848−2857.

(61) Bell, S. R.; Groves, J. T. A Highly Reactive P450 Model Compound I. *J. Am. Chem. Soc.* **2009**, *131*, 9640−9641.

(62) Krebs, C.; Price, J. C.; Baldwin, J.; Saleh, L.; Green, M. T.; Bollinger, J. M., Jr. Rapid Freeze-Quench ^{57}Fe Mössbauer Spectroscopy: Monitoring Changes of an Iron-Containing Active Site during a Biochemical Reaction. *Inorg. Chem.* **2005**, *44*, 742−757.

(63) Sastri, C. V.; Lee, J.; Oh, K.; Lee, Y. J.; Lee, J.; Jackson, T. A.; Ray, K.; Hirao, H.; Shin, W.; Halfen, J. A.; Kim, J.; Que, L.; Shaik, S.; Nam, W. Axial ligand tuning of a nonheme iron(IV)−oxo unit for hydrogen atom abstraction. *Proc. Natl. Acad. Sci. U. S. A.* **2007**, *104*, 19181−19186.

(64) Company, A.; Gómez, L.; Costas, M. Bioinspired Non-heme Iron Catalysts in C−H and C═C Oxidation Reactions. In *Iron-Containing Enzymes*; Visser, S. P. d., Kumar, D., Eds.; RSC Publishing: Cambridge, 2011.

(65) Mader, E. A.; Davidson, E. R.; Mayer, J. M. Large Ground-State Entropy Changes for Hydrogen Atom Transfer Reactions of Iron Complexes. *J. Am. Chem. Soc.* **2007**, *129*, 5153−5166.

(66) Evans, M. G.; Polanyi, M. Inertia and driving force of chemical reactions. *Trans. Faraday Soc.* **1938**, *34*, 11−24.

(67) Wang, D.; Zhang, M.; Bühlmann, P.; Que, L. Redox Potential and C−H Bond Cleaving Properties of a Nonheme Fe^{IV}═O Complex in Aqueous Solution. *J. Am. Chem. Soc.* **2010**, *132*, 7638−7644.

(68) Usharani, D.; Lacy, D. C.; Borovik, A. S.; Shaik, S. Dichotomous Hydrogen Atom Transfer vs Proton-Coupled Electron Transfer During Activation of X−H Bonds (X = C, N, O) by Nonheme Iron−Oxo Complexes of Variable Basicity. *J. Am. Chem. Soc.* **2013**, *135*, 17090−17104.

(69) Mittra, K.; Green, M. T. Reduction Potentials of P450 Compounds I and II: Insight into the Thermodynamics of C−H Bond Activation. *J. Am. Chem. Soc.* **2019**, *141*, 5504−5510.

(70) Postils, V.; Company, A.; Solà, M.; Costas, M.; Luis, J. M. Computational Insight into the Mechanism of Alkane Hydroxylation by Non-heme Fe(PyTACN) Iron Complexes. Effects of the Substrate and Solvent. *Inorg. Chem.* **2015**, *54*, 8223−8236.

(71) Wang, Y.; Janardanan, D.; Usharani, D.; Han, K.; Que, L.; Shaik, S. Nonheme Iron Oxidant Formed in the Presence of H2O2 and Acetic Acid Is the Cyclic Ferric Peracetate Complex, Not a Perferryloxo Complex. *ACS Catal.* **2013**, *3*, 1334−1341.

(72) Chen, H.; Lai, W.; Shaik, S. Exchange-Enhanced H-Abstraction Reactivity of High-Valent Nonheme Iron(IV)-Oxo from Coupled Cluster and Density Functional Theories. *J. Phys. Chem. Lett.* **2010**, *1*, 1533−1540.

(73) Hirao, H.; Kumar, D.; Que, L.; Shaik, S. Two-State Reactivity in Alkane Hydroxylation by Non-Heme Iron−Oxo Complexes. *J. Am. Chem. Soc.* **2006**, *128*, 8590−8606.

(74) Groves, J. T.; Adhyam, D. V. Hydroxylation by cytochrome P-450 and metalloporphyrin models. Evidence for allylic rearrangement. *J. Am. Chem. Soc.* **1984**, *106*, 2177−2181.

(75) Oloo, W. N.; Feng, Y.; Iyer, S.; Parmelee, S.; Xue, G.; Que, L. Cyclohexene as a substrate probe for the nature of the high-valent iron-oxo oxidant in Fe(TPA)-catalyzed oxidations. *New J. Chem.* **2013**, *37*, 3411−3415.

(76) Shul'pin, G. B.; Süss-Fink, G.; Smith, J. R. L. Oxidations by the System "Hydrogen Peroxide - Manganese(IV) Complex - Acetic Acid" - Part II. *Tetrahedron* **1999**, *55*, 5345−5358.

(77) Jiang, Y.; He, X.; Ortiz de Montellano, P. R. Radical Intermediates in the Catalytic Oxidation of Hydrocarbons by Bacterial and Human Cytochrome P450 Enzymes. *Biochemistry* **2006**, *45*, 533−542.

(78) Cho, K.-B.; Hirao, H.; Shaik, S.; Nam, W. To rebound or dissociate? This is the mechanistic question in C−H hydroxylation by heme and nonheme metal−oxo complexes. *Chem. Soc. Rev.* **2016**, *45*, 1197−1210.

(79) Pangia, T. M.; Davies, C. G.; Prendergast, J. R.; Gordon, J. B.; Siegler, M. A.; Jameson, G. N. L.; Goldberg, D. P. Observation of Radical Rebound in a Mononuclear Nonheme Iron Model Complex. *J. Am. Chem. Soc.* **2018**, *140*, 4191−4194.

(80) Drummond, M. J.; Ford, C. L.; Gray, D. L.; Popescu, C. V.; Fout, A. R. Radical Rebound Hydroxylation Versus H-Atom Transfer in Non-Heme Iron(III)-Hydroxo Complexes: Reactivity and Structural Differentiation. *J. Am. Chem. Soc.* **2019**, *141*, 6639−6650.

(81) Serrano-Plana, J.; Aguinaco, A.; Belda, R.; García-España, E.; Basallote, M. G.; Company, A.; Costas, M. Exceedingly Fast Oxygen Atom Transfer to Olefins via a Catalytically Competent Nonheme Iron Species. *Angew. Chem., Int. Ed.* **2016**, *55*, 6310−6314.

(82) Sankaralingam, M.; Lee, Y.-M.; Jeon, S. H.; Seo, M. S.; Cho, K.-B.; Nam, W. A mononuclear manganese(III)−hydroperoxo complex: synthesis by activating dioxygen and reactivity in electrophilic and nucleophilic reactions. *Chem. Commun.* **2018**, *54*, 1209−1212.

(83) Kim, S. J.; Latifi, R.; Kang, H. Y.; Nam, W.; de Visser, S. P. Activation of hydrocarbon C−H bonds by iodosylbenzene: how does it compare with iron(IV)−oxo oxidants? *Chem. Commun.* **2009**, 1562−1564.

(84) George, G. N. *EXAFSPAK*; Stanford Synchrotron Radiation Laboratory, Stanford Linear Accelerator Center: Stanford, CA, 2000.

(85) Wojdyr, M. Fityk: a general-purpose peak fitting program. *J. Appl. Crystallogr.* **2010**, *43*, 1126−1128.

(86) ASTM E1840−96: Standard Guide for Raman Shift Standards for Spectrometer Calibration; ASTM International, 2007; DOI: 10.1520/E1840-96R07.

(87) Menges, F. *Spectragryph*, Version 1.2.10; 2018. http://www.effemm2.de/spectragryph/ (accessed on March 24, 2019).

DOI: 10.1021/jacs.9b05758
J. Am. Chem. Soc. XXXX, XXX, XXX−XXX